ABSTRACT

Title of Thesis: PERFORMANCE CHARACTERIZATION OF POOL BOILING ON INNOVATIVE FOAMS AND MICRO STRUCTURED SURFACES - APPLICATION TO DIRECT IMMERSION COOLING OF ELECTRONICS

Degree candidate: Lewis Elliot Gershen

Degree and year: Master of Science, 2003

Thesis directed by: Professor Michael Ohadi
Department of Mechanical Engineering
Associate Professor Jungho Kim
Department of Mechanical Engineering

This thesis is an experimental investigation of the thermal performance during boiling on copper foam and copper-finned microstructures as a thermosyphon evaporator. Copper foam is an open-celled porous media with interconnected copper ligaments of thermal conductivity up to 1.51 W/(cm^2·K). The high thermal conductivity of this type of copper foam allows heat to rapidly spread through the foam causing widespread boiling. The boiling allows large transfers of energy from the heater (the source) to the working fluid (sink) with a low temperature difference between the heated surface and the working fluid.

The thermal performance of the copper foams was investigated as a function of parametric values of foam height, pore density (pores per inch - PPI), and porosity. Data showed the pore density and porosity of the foam significantly affected heat transfer by changing the pore sizes and ligament sizes while thickness in the range of 1 to 5 mm had little effect on thermal performance. Surface tension is shown by dimensionless analysis

to be the dominating force within the foam. The data also indicated the heat transfer coefficient for boiling HFE-7100 from copper foam ranged from 2,000 to 9,000 W/(m^2·K). The copper foams provided significant heat transfer from the source. For example, copper foams provided heat loads up to 70 W/cm^2 at 90 ^oC superheat.

The second set of experiments in the present study involved testing of micro-finned structures. For such surfaces the important parameters we paid attention to were fin density (fins per inch) and aspect ratio (ratio of channel height to channel width) of the copper-finned microstructures. The data showed that aspect ratio and fin density substantially affect heat transfer performance through different channel cross-section sizes. The heat transfer provided by the micro-finned structures was substantially enhanced. For example, copper-finned microstructures provided heat loads up to 43 W/cm^2 at 20 ^oC superheat.

In this thesis, many chapters will discuss the reasoning behind this study and the results of it. The first chapter will cover the motivation and background information for this work. The next chapter discusses the experimental setup and how the results were obtained. The third chapter will review the results of the copper foams and discuss the cause of the results. The fourth chapter discusses the thermal performance of micro-finned structures. Finally, the conclusions of this study and suggested future work will be presented in the last chapter.

PERFORMANCE CHARACTERIZATION OF POOL BOILING ON INNOVATIVE FOAMS AND MICRO STRUCTURED SURFACES--APPLICATION TO DIRECT IMMERSION COOLING OF ELECTRONICS

by
Lewis Elliot Gershen

Thesis submitted to the Faculty of the Graduate School of the University of Maryland, College Park in partial fulfillment of the requirements for the degree of
Master of Science
2003

Advisory Committee:

Professor Michael Ohadi, Chair
Associate Professor Jungho Kim, Chair
Professor Reinhard Radermacher

ACKNOWLEDGMENTS

First and foremost, I would like to thank my loved ones for their support and encouragement during this endeavor. I also want to thank my advisors, Dr. Michael Ohadi and Dr. Jungho Kim, for their support throughout the project. I would like to thank Dr. Jianwei Qi for his insight of the material. I especially want to thank Dr. Serguei Dessiatoun for his encouragement, insight on the technology, and help with the design of the testing rig. Also, I would like to thank Bernie LaFrance who machined various components of the test rig. This project was supported by the CALCE department at the University of Maryland under Project #C03-15. Finally, I am grateful to Brazeway, Inc.™ and Wolverine Tube, Inc.™ for generously providing copper foams and copper-finned microstructures, respectively.

TABLE OF CONTENTS

LIST OF TABLES

LIST OF FIGURES

NOMENCLATURE

Symbols

Bo	Bond number
Ca	Capillary number
d	Diameter [m]
g	Acceleration due to gravity [m/s^2]
Gr	Grashof number
h	Heat transfer coefficient [$W/cm^2 \cdot K$], Enthalpy [J/kg]
k	Thermal conductivity [W/cm·K]
l	Length [m]
$\dot{m}$	Mass flux [kg/s]
P	Pressure [Pa]
q	Heat [W]
q''	Heat flux [W/cm^2]
R	Thermal resistance [K/W]
Re	Reynolds number
T	Temperature [^oC] (unless specified as [K])
u	Velocity [m/s]
V	Volume [m^3]
A	Surface area

Greek

μ	Viscosity [kg/(m·s)]

ν	Kinematic viscosity [m^2/s]
ρ	Density [g/cm^3]
σ	Surface tension [N/m], standard deviation
ξ	Porosity

Subscripts

bulk	Ambient or bulk material
Cu	Copper
CuFoam	Copper foam material
CuPlate	Copper plate
fg	Latent change of state from liquid to gas
sat	Saturation
solid	Solid material
wall (surface)	Wall surface
v	vapor
l	liquid
avg	Average
nichrome	Nichrome material
solder	Solder material
Max	maximum
outside	outside area

Abbreviations

CHF	Critical heat flux
H	Height
FPI	Fins per linear inch
PPI	Pores per linear inch
TC	Thermocouple

1. INTRODUCTION

1.1 The Need for New Electronic Cooling Techniques

The use of electronic components in military equipment, vehicles and computers is becoming increasingly pervasive. New technology uses faster processors, wider busses and higher bandwidths. The electronics used in military equipment and other high temperature electronics, such as those found near the engine compartment of a vehicle, are compact and dissipate higher levels of heat. Power densities and heat dissipation of processors have increased nearly two-fold (Patterson, 2002). For example, vehicles and military equipment (e.g. radar, missiles) are primarily controlled electronically rather than by mechanical devices. Manufacturers are introducing entertainment devices such as televisions, compact disc players, and navigation systems into automobiles. These electronics are impacted upon by harsh environments caused by high temperatures inside vehicles. Electronics in military equipment are used to control calibrated machines, radar, and weapons such as missiles. Therefore, it is necessary to control these high-temperature environments, carefully managing performance, reliability, and cost.

Personal computers will use smaller processors generating greater amounts of heat, which will require cooling methods beyond the capability of current methods. Without new cooling methods these processors will be destroyed. The processors must be maintained at 85 °C or less to remain reliable. Power density cooling methods must be developed to dissipate as much as 100 W/cm^2 (Kalo, 2002). It is necessary to control these environments while maintaining performance, presenting reliability, and controlling cost. A promising method of cooling such electronics is the use of pool boiling with a dielectric fluid accompanied by an enhanced heat transfer microstructure (Examples of such microstructures include foams and finned microstructures studied in this thesis).

For example, an evaporator can be bonded to the top of the processor to remove the processor's dissipating heat.

1.2 Motivation

The potential of porous copper foam materials and micro-finned surfaces as evaporators in a thermosyphon for the purpose of thermal management was investigated.

Thermosyphons dissipate heat using working fluids that become two-phase (liquid and vapor). A thermosyphon consists of a condenser, evaporator, and an adiabatic chamber between the two. Vapor forms at the evaporator and rises due to buoyancy. When the vapor reaches the top of the chamber, it condenses and latent heat is released into the condenser. The condensate then returns to the evaporator by the force of gravity. An example of a currently used thermosyphon can be seen in Figure 1.1 below.

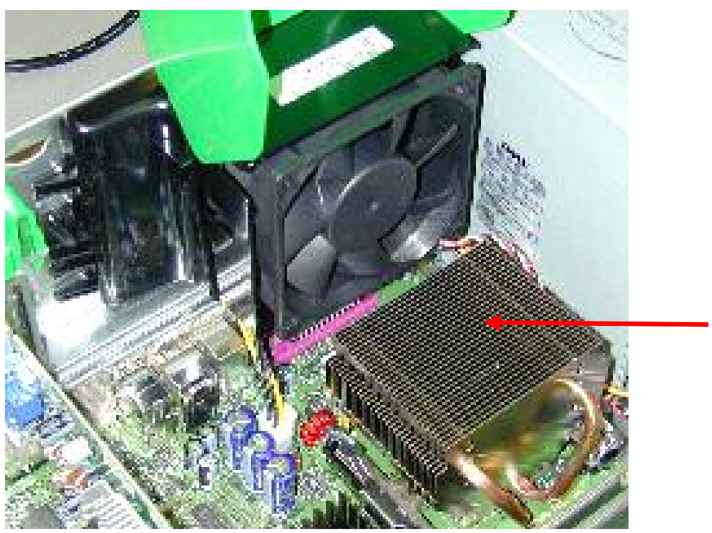

Figure 1.1: Thermosyphon in computers (Coursey, 2003).

The thermal performance of copper foams under varying conditions was investigated because limited research literature describing its thermal performance existed. Copper foams of different porosities, pore densities and thicknesses were studied to determine the variation in thermal performance due to these physical properties.

There is also virtually no data describing the thermal performance of copper-finned microstructures. Since this was a new type of evaporator, the thermal performance was studied and compared to the thermal performance of the copper foams.

1.3 Literature Review

Literature exists on pool boiling in porous media, but is limited on the thermal performance of copper-finned microstructures.

In Ramaswamy et al.'s (2003) study of microfabricated silicon evaporators, it was shown that increased pore sizes from 90 to 320 μm increased heat transfer at low to intermediate superheats. At higher superheats, however, all pore sizes had similar performance. Furthermore, it was found that at a higher pore density better thermal performance was evident at all superheats. Ramaswamy et al.'s experiments indicated that increasing the thickness of the evaporator increases heat dissipation at low and high superheats, but at an intermediate superheat (10 K), he found that thicker evaporators performed the same as thinner evaporators. He attributed this to a fin effect where boiling occurs on the outside of the evaporator.

In Coursey's (2003) study of graphite foam in FC-72 and FC-87 (two different dielectric fluids produced by 3M™), research indicated that thicker evaporators decrease thermal performance. He suggests that moving the top surface further away from the heated wall, which causes boiling to occur only on the evaporator's surfaces, causes this lower thermal performance. He also stated that heat transfer is reduced due to high surface tension force in foams, which reduces bubble departure frequency. Coursey stated that decreased porosity, e.g. lower pore volume relative to total volume, increased the thermal performance because increased foam material raised the thermal conductivity. Finally, he asserted that the mass flux of the fluid can be estimated by assuming heat transferred within the foam is a result of latent heat transfer.

Athreya et al. (2002) studied pool boiling of aluminum foam heat sinks in FC-72 with varying orientations, pore density, and foam thickness. He found that the critical heat flux decreases and thermal performance first decreases but then increases as thickness increases for lower PPI (5 PPI) foams oriented horizontally. This indicated that an intermediate thickness, thermal performance is at its lowest during high flux nucleate boiling. Nucleate boiling is not enhanced beyond a certain thickness because pore density and porosity limits the foam's volume. He observed a decreased superheat jump in the transition from nucleate to film boiling as foam thickness increases.

In 1976, Wong et al. studied thermal equilibrium in liquid saturated porous media. He found that thermal equilibrium exists between the solid and fluid within the porous media. Therefore, there was virtually no convection heat transfer in the interior of the foam. Latent heat transfer was the only mode of heat transfer in the interior of the porous media.

Thermosyphon evaporators have been tested for several years, but the thermal performance of metal foams is of particular current interest because metal foams are made of highly thermally conductive material. Copper foam is typically produced by means of 4 processes (Coursey, 2003):

1. Stirring a foaming agent into a liquid alloy.
2. Forming metal powder with some type of foaming agent.
3. Bubbling gas through a molten Al-SiC or Al-Al_2O_3 alloy.

4. Investment casting from a ceramic mold made from some polymer foam precursor.

The thermal conductivity of foam depends on thermal conductivity of the solid and the densities of the foam and solid shown below:

$$k_{foam} \le \frac{k_{solid}\,\rho_{foam}}{\rho_{solid}} \qquad \text{(1.1, Coursey, 2003)}$$

Due to misalignment of material crystals and the addition of grain boundaries, the thermal conductivity of foam is reduced. The thermal conductivity is always less than it would be if it were scaled on the relative density alone. As the porosity increases, the effects of misaligned crystals and grain boundaries are magnified and vary widely depending on the processing method (Coursey, 2003).

1.3.1 Copper Foams

Copper foams used in this research study were provided by Brazeway, Inc.™. The foam samples are characterized by their pores per inch (PPI), porosity (volume of pores relative to total volume) and thickness (height). The porosity takes into account the size of the pores and ligaments between each pore. Foams can be made of any metal that can be broken down to powder, but copper is particularly useful because of its high thermal conductivity. Therefore, copper foams were selected for this study.

1.3.2 Copper-finned Microstructures

Copper-finned microstructures, provided by Wolverine Tube, Inc.™, were used in this study. They proved to be highly thermally conductive. Since they have small channels between fins without impeding objects (e.g. ligaments), greater capillary siphoning of the dielectric fluid via thermocapillary effects can be used to obtain higher heat transfer loads relative to aluminum or copper foams. Copper-finned microstructures are characterized by their fin density (which is measured in fins per inch - FPI), their channel width, and channel height. Pool boiling on eight different copper-finned microstructures was performed. An example of the physical properties of these copper-finned microstructures is shown in Table 1.1.

Table 1.1: Wolverine Tube, Inc.™ copper fin properties.

Fin Density	185 FPI
Channel Height	0.024” (0.6096 mm)
Channel Width	0.00271”
Thermal Conductivity	393 W/m·K

The experiments performed showed that copper-finned microstructures had about 150% higher heat transfer than the highest performance copper foam at low superheats. Copper-finned microstructures exhibited thermal performances between 20 W/cm^2 and 45 W/cm^2 at 10 ^{o}C superheat while copper foams exhibited thermal performances at approximately 13 W/cm^2 at 10 ^{o}C superheat. Its average volume was 18% of that of the copper foam (the volume of the finned microstructure is 0.06 cm^3 while the copper foam has an average volume of 0.32 cm^3). Therefore, the copper fins’ thermal management properties and physical characteristics indicated a potentially promising future for heat transfer applications in high temperature electronics, automobiles, and military electronics. However, at the present time more research is necessary on this new finned microstructure acting as channels for HFE-7100.

1.4 Physics of Pool Boiling

When the surface temperature T_s exceeds the saturation temperature T_{sat} corresponding to the liquid pressure, boiling occurs. Bubble departure is believed to enhance convective wall heat transfer during pool boiling (Incropera et al., 2001). Therefore, increasing the temperature of the solid surface agitates the fluid resulting in boiling. The pool boiling process is made up of four regimes that include natural convection, nucleate boiling, transition boiling and film boiling. The behavior of the boiling curve in each of these regimes is shown in Figure 1.2.

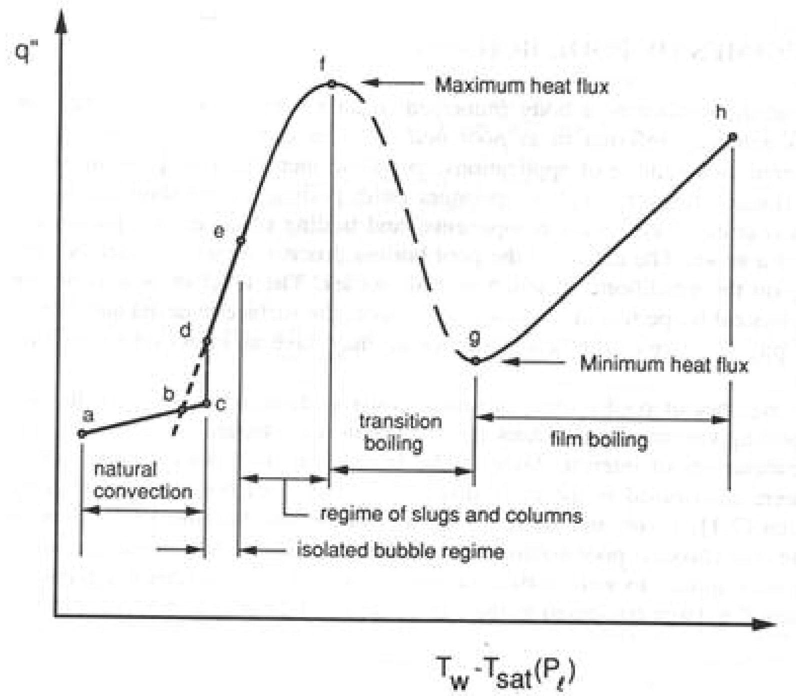

Figure 1.2: Typical pool-boiling curve (Carey, 1992).

1.4.1 Natural Convection

At low superheats, natural convection exists. At these superheats, nucleation sites may not be active and heat is transferred to the ambient liquid from the wall surface by natural convection as shown in Figure 1.3. The nucleation sites are deactivated by penetration of the colder bulk liquid into cavities of the material, which prohibits bubbles from growing and releasing. Some vapor may exist, but the interior vapor pressure is not high enough (relative to the vapor pressure) to allow the bubble embryo to grow and nucleate. As a result, boiling occurs at wall temperatures above the saturation temperature of the fluid.

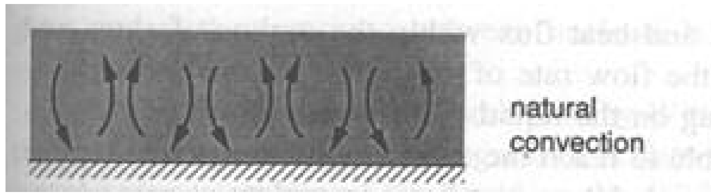

Figure 1.3: Schematic of natural convection and the onset of boiling (Carey, 1992).

At the boiling point, bubbles start to form when more heat is generated at the surface. This allows the nucleation sites to become active as shown in Figure 1.4. The conditions necessary to activate the nucleation sites are characterized in Equation 1.2 where r* is the critical radius (which depends on the contact angle and cavity half angle during bubble embryo growth), R is the cavity mouth radius and r is the bubble embryo radius.

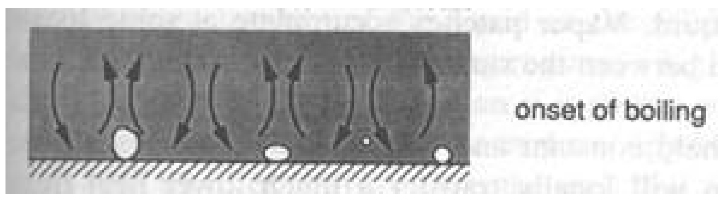

Figure 1.4: Schematic of the onset of boiling (Carey, 1992).

$$T_l - T_{sat}(P_l) > \frac{2\sigma T_{sat}(P_l) v_{lv}}{h_{lv} r^*}$$

$$\frac{R}{r} > r^* \qquad \text{(1.2, Carey, 1992)}$$

At the boiling point, the liquid adjacent to the wall is heated, creating a thermal boundary layer by transient conduction as shown in Figure 1.5 below. In the thermal boundary layer, heat transfer occurs solely by molecular diffusion. Beyond the thermal boundary layer, however, vigorous turbulent transfer causes a uniform bulk temperature to occur. The conditions necessary for bubble embryo growth are characterized in Equation 1.3 where θ represents the superheat and θ_w is the wall temperature, δ_t is the thermal boundary layer thickness, and t is the time.

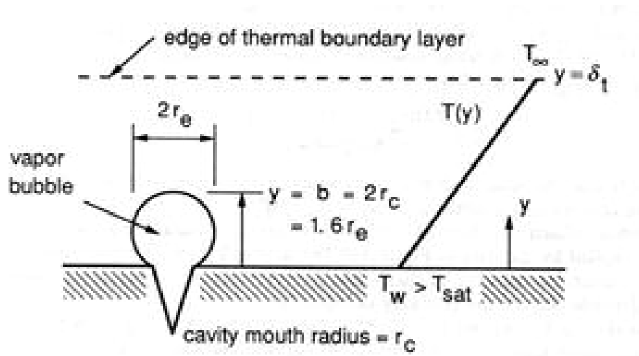

Figure 1.5: Hsu's model of bubble embryo growth (Carey, 1992).

$$\frac{\theta}{\theta_w} = \frac{\delta_t - y}{\delta_t} + \frac{2}{\pi}\sum_{n=1}^{\infty}\frac{\cos n\pi}{n}\sin\left[n\pi\left(\frac{\delta_t - y}{\delta_t}\right)\right]e^{-n^2\pi^2\left(\frac{\alpha t}{\delta_t^2}\right)} \qquad \text{(1.3, Carey, 1992))}$$

1.4.2 Nucleate Boiling

Nucleate boiling occurs when bubbles begin to form on the heated surface. In the first regime of nucleate boiling, isolated bubbles form at nucleation sites, which depart from the heated surface as seen in Figure 1.6. This allows the ambient fluid to mix near the surface, increasing the heat transfer coefficient. Most heat transfer in this regime is from direct transfer between the solid and liquid via the motion of the liquid. Vapor within the bubbles does not play a major role in the actual heat transfer.

At higher heat fluxes, however, nucleation sites become more numerous. The active nucleation sites are close enough together so that bubbles begin to interfere with each other. In this regime, vapor is being produced so quickly that bubbles merge into columns or slugs as seen in Figure 1.6. This continues to occur as heat flux rises until the heat flux reaches the critical heat flux (CHF).

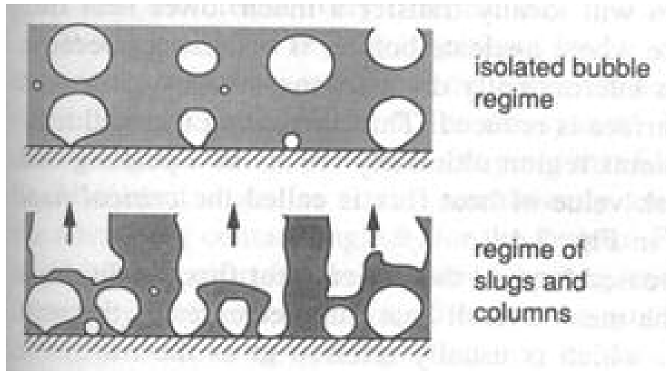

Figure 1.6: Schematic of both regimes in nucleate boiling (Carey, 1992).

1.4.3 Critical Heat Flux

The critical heat flux (CHF) is where the boiling curve heat flux reaches a maximum while transitioning between nucleate and transition boiling. There are many hypotheses concerning the reason for CHF. A model proposed by Zuber (an extension of Kutateladze's model) seems to fit CHF data the best. In this model, bubbles coalesce at the surface to form vapor columns. CHF occurs when the interface of the large vapor columns leaving the surface become Helmholtz-unstable, e.g. when the interface of the vapor columns makes the diameter of the vapor columns to be $\lambda_d/2$ (λ_d is the Taylor instability wavelength). The instability prevents liquid from contacting the heated surface between the vapor columns. A vapor film then forms on the surface, causing CHF to occur.

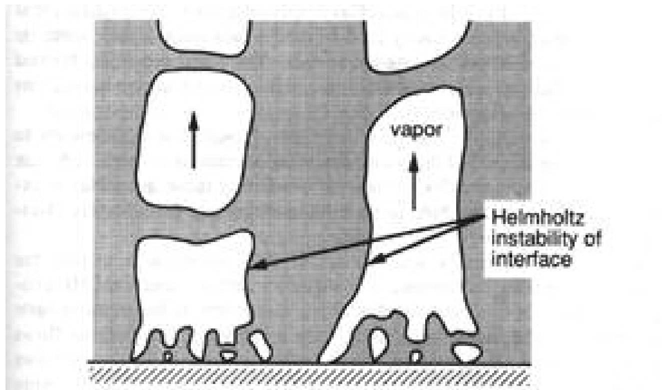

Figure 1.7: Helmholtz instability CHF mechanism (Carey, 1992).

1.4.4 Transition Boiling

During transition boiling, a reduction in heat flux and a significant increase in superheat are observed. As superheat increases, bubble formation becomes more rapid, and a film of vapor increasingly covers the heated surface (see Figure 1.8 below). Since the vapor has a lower thermal conductivity than the liquid, the heat transfer rate decreases rapidly. In this region, fluctuations between film boiling and nucleate boiling occur. As wall superheat intensifies, film boiling increases while nucleate boiling decreases.

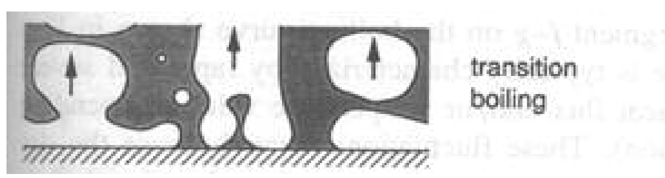

Figure 1.8: Schematic of transition boiling (Carey, 1992).

1.4.5 Film Boiling

Film boiling occurs at the Leidenfrost point, when heat flux reaches a minimum after CHF. At this point, a vapor blanket completely covers the heated surface as seen in Figure 1.9. Heat is transferred from the surface to the liquid only by conduction and radiation but because of an increase in surface temperature radiation is more significant. Superheat in this regime can be high enough to melt or destroy the surface. However, it is imperative to know when CHF occurs so surface burnout can be prevented.

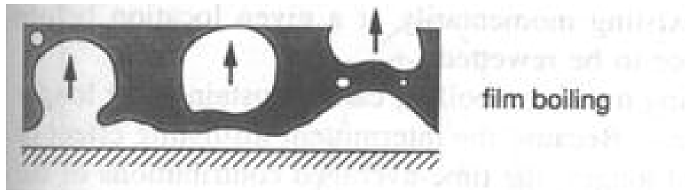

Figure 1.9: Schematic of film boiling (Carey, 1992).

1.5 Current Study

The current study focused on exploring the potential of using copper foams and copper-finned microstructures with varying parameters for direct immersion cooling of electronic chips. Furthermore, the effects of foam height, width, density, porosity, copper-finned microstructure channel aspect ratio (ratio of channel height to channel width), fin density, and wall temperature were examined in various experiments. All samples were tested at 60 ºC, the saturation temperature for HFE-7100 at 1.0 atm.

Base line tests were conducted to establish a reference point by testing the thermal performance of a flat nichrome plate and a scratched-copper plate. After the base line was established, copper foams with varying porosities, pores per inch (30, 45, 60, 80 and 100 PPI) and thicknesses (1 to 5 mm) were tested. Then, tests of copper-finned microstructures with varying fin densities (185, 212, 280, 320, 508, and 635 FPI) and aspect ratios were conducted.

2. EXPERIMENTAL APPARATUS

2.1 Introduction

The thermal performance of each of the samples was determined by comparing the heat transfer and accompanying superheat of the samples under the same testing conditions. Each sample's thermal performance and superheat were measured and graphed, giving a boiling curve.

In order to provide identical testing conditions for each sample, a test section was built. The test section was designed to best handle the working (cooling) fluid and operating temperature and pressure. The working fluid was Novec^{TM} HFE-7100 hydrofluoroether (HFE) fluid, the operating saturation temperature was 60 ^{o}C, and the saturation pressure was 1.0 atmosphere.

2.2 Modules of the Experiment

The modules of the experiment, shown in Figure 2.1, were as follows:

- Test Section (shown in Figure 2.2)
    - Main chamber
    - Heater
    - Foam/fin sample
    - Working Fluid
- Control systems
- DC power supply
- Measurement devices

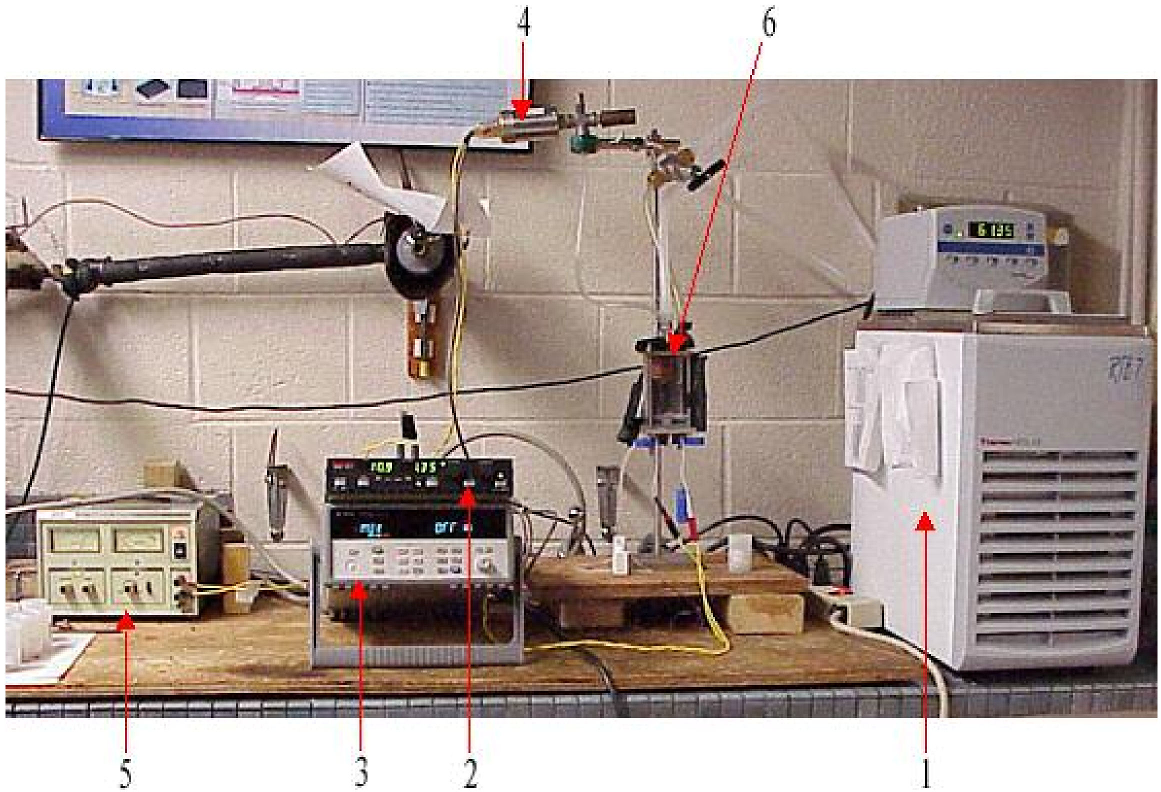

1. NESLAB™ RTE-7 Digital Plus Chiller
2. Sorenson DLM150-4M9G DC power supply for heater
3. Agilent digital multimeter to measure temperatures and pressure
4. Pressure transducer
5. Pressure transducer's power supply
6. Testing chamber

Figure 2.1: Modules of the experiment.

2.2.1 Test Section

2.2.1.1 Main Chamber

The main chamber held the working fluid and sample. The top of the chamber was a 195 x 195 x 52 mm copper block, sealed at the top of the glass enclosure with a Viton-141 O-ring. The bottom of the chamber was an aluminum base plate of the same size as the copper block, but with a hole in its center to house the heater and sample. The aluminum base was sealed to the bottom of the glass enclosure with a Viton-141 O-ring. The glass enclosure had a height, diameter and wall thickness of 101.6 mm, 63.5 mm, and 3.175 mm, respectively. The test sample was visible during testing within the glass enclosure, as shown in Figure 2.2.

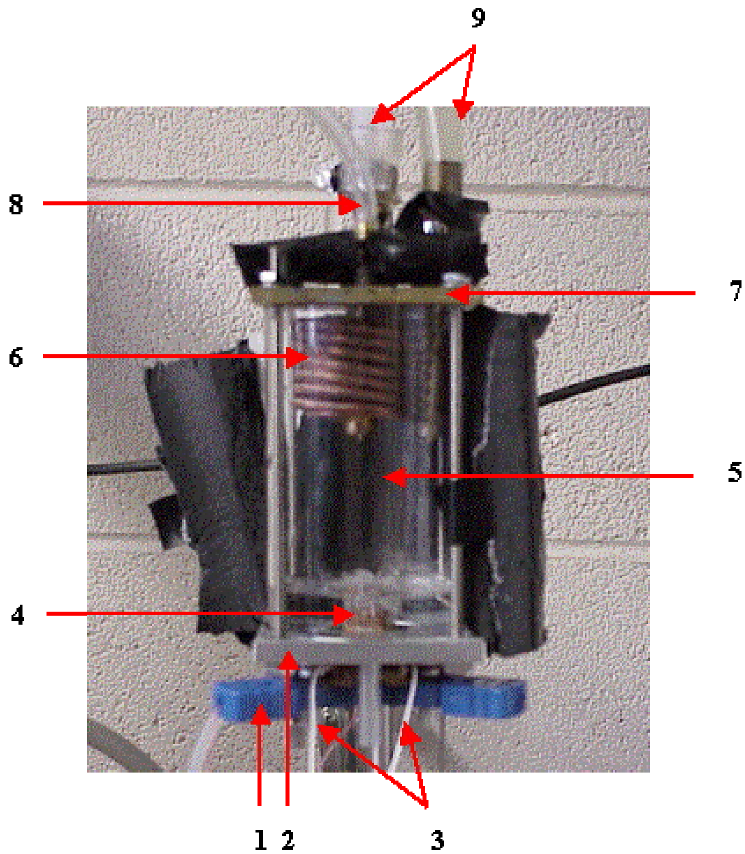

1. Thermocouples
2. Aluminum base plate
3. Power supply wires
4. Foam/fin sample
5. Glass enclosure
6. Condenser
7. Copper base plate
8. Pressure transducer tube
9. Water inlet/outlet for copper coils

Figure 2.2: Cross-sectional view of the test section.

2.2.1.2 Heater

The heater, shown in Figure 2.4 and Figure 2.5, was designed and built by Rinc, Inc. It consisted of a resistor that supplied heat to a 10 mm^2 square copper block. The top of the copper block was fusion bonded to a 0.07 mm thick nichrome plate. Nichrome was chosen because it is similar to stainless steel in its properties except that its low thermal conductivity helps to prevent radial heat loss. The schematic of the heater (Figure 2.3) illustrates the location of holes in the copper-heating block for the thermocouples. These holes located 1 mm below the nichrome plate, were 1 mm in diameter and had a depth 5 mm.

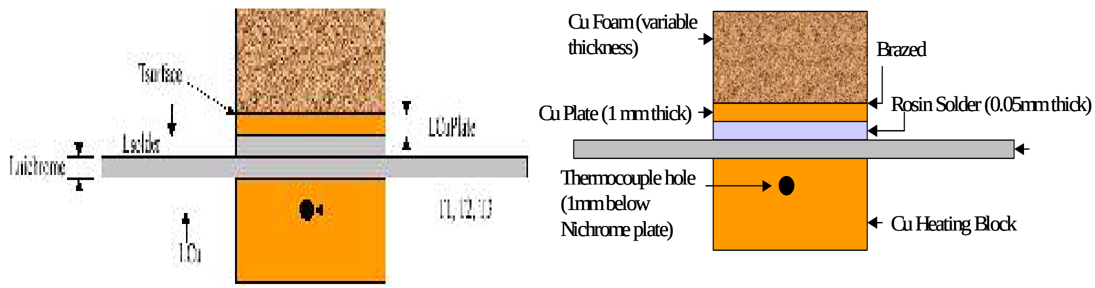

Figure 2.3: Schematic of the heater.

The nichrome plate, best seen in Figure 2.5, was a circular diaphragm with thickness 0.07 mm and thermal conductivity 13.4 W/(m·K) (Goodfellow, 2003). The top of the nichrome plate had a 10 mm x 10 mm non-oxidized section for placement of the samples.

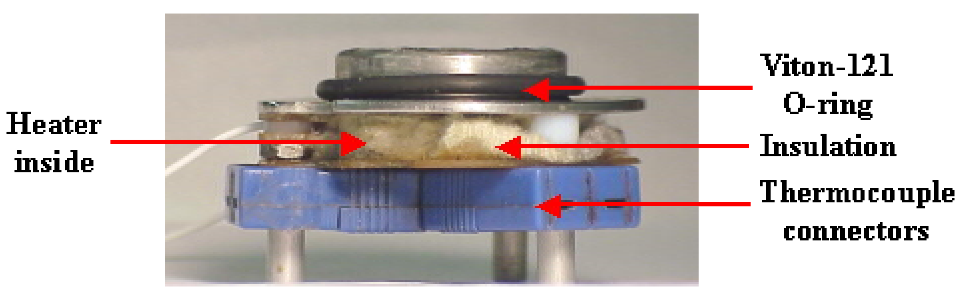

Figure 2.4: Side view of the heater assembly.

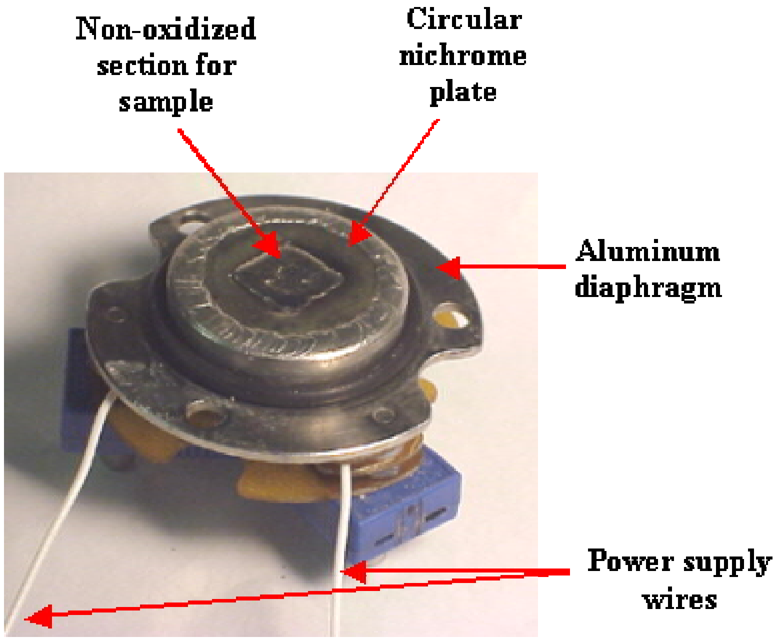

Figure 2.5: Top view of the heater assembly.

2.2.1.3 Foam

Each copper foam sample was brazed to a 10 x 10 x 0.77 mm copper base plate by cleaning the sample and the plate, clamping them together, and placing them into a vacuum furnace. The temperature of the furnace was raised to within 0.5 – 0.8 ^{o}C of the melting temperature of the foam and plate. The foam and copper plate began to fuse together and then were cooled to room temperature in the furnace.

The bottom of the copper base plate was rosin soldered to the non-oxidized area on top of the nichrome surface of the heater. Flux and rosin solder consisting of 60% tin and 40% lead with a thermal conductivity of 50 W/(m·K) and a melting point of 178 ^{o}C (Goodfellow, 2003) was applied to the 10 mm^2 square non-oxidized section on top of the nichrome surface. The heater temperature was raised to a minimum of 178 ^{o}C to melt the solder, creating an evenly distributed layer on the non-oxidized section of the nichrome surface. The heater was then cooled to approximately 90 ^{o}C. At this point the bottom of the copper base plate was fluxed and aligned with the non-oxidized portion of the nichrome surface. A spring was placed on top of the copper foam sample to apply even, steady pressure. The solder between the copper base plate and the nichrome plate was melted and compressed until a 0.05 mm thick solder layer was created. A wooden toothpick was used to remove any excess solder. Finally, the heater was turned off and the solder was cooled below its melting temperature. The spring was removed and the sample was rinsed with ethanol. The solder thickness was confirmed by measuring the first few samples under a microscope. All of the measured solder thicknesses were found to be 0.05 mm. Since the soldering process was repeated for every sample, the solder thickness was assumed to be the uniform throughout all samples tested.

The parameters of the tested copper foams are tabulated in Table 2.1 below.

Table 2.1: Parameters of copper foams tested.

PPI	Height (mm)	Porosity
30	5	0.945
45	1	0.826
45	3	0.876
45	5	0.920
60	2	0.779
60	2	0.854
60	2	0.938
60	5	0.938
80	2	0.902
100 (fusion bonded)	1	0.846

2.2.1.4 Copper-finned Microstructures

The copper-finned microstructures were rosin soldered directly to the 10 mm x 10 mm non-oxidized area on the top of the nichrome plate in the same manner as the copper base plates of the copper foams. To avoid filling the channels of the finned microstructure with solder through capillary effects, carbon oxides were applied with a torch to generate a thin oxide layer on top of the copper-finned microstructures. The copper-finned microstructure was then placed on top of the cooled solder and aligned with the non-oxidized area of the nichrome surface. As with the copper foams, a spring was placed on top of the copper-finned microstructure to maintain even and steady pressure. Power was applied to the heater, melting the solder and bonding the copper-finned microstructure to the nichrome plate with a 0.05 mm-thick solder layer. A wooden toothpick was used to again remove the excess solder. The heater was then turned off which cooled the solder below its melting point. After the solder cooled the spring was removed. The oxide layer was removed with hexanes and ethanol.

The parameters of copper-finned microstructures tested are listed in Table 2.2 below.

Table 2.2: Parameters of copper-finned microstructures tested.

Sample	FPI	Channel Cross Section (cm^2)	Aspect Ratio (height/width)	Fin Thickness (cm)
1	212	0.0742	22	0.060043
2	280	0.0023	28	0.081672
3	320	0.0000	N/A	0.079375
4	508	0.0022	85	0.000000
5	635	0.0026	180	0.036196
6	212	0.0341	10	0.060043
7	212	0.0297	9	0.060043
8	185	0.0420	9	0.068835

2.2.1.5 Working Fluid

The question of which fluid to use was carefully considered in this project. Possible fluids considered were water, R-134a, FC-72, and HFE-7100. Water is not useful in direct immersion for electronic cooling due to its low dielectric strength. Therefore, it was not used. R-134a was not used because it is more toxic than HFE and FC fluids. FC-72 has been in common use as a dielectric fluid for thermosyphon cooling for several years, but it has a higher toxicology, a higher cost and lower latent heat than HFE-7100. Therefore, it was not chosen for this project. The cooling fluid used was HFE-7100, a new Novec™ hydrofluoroether (HFE) fluid. HFE-7100 was ideal because it has a high dielectric strength, high heat of vaporization, and low boiling point. Apart from these technical factors, HFE-7100 is available at a low cost and is commonly used in the electronic cooling industry. Table 2.3 lists all relevant characteristics of HFE-7100 as well as the characteristics of other dielectric fluids.

Table 2.3: Properties of common cooling fluids that were considered (3M™, 2003).

Property	HFE-7100	FC-72	R-134a	Water
Molecular Weight	250	338	102	18
T_{sat} (^oC)	60	56	-26.09	100
T_{sat} (^oC)	-135	-75	-104.3	0
ρ_l (kg/m^3)	1,373	1,680	1,377	958.4
σ (N/m)	0.0104	0.01	0.01544	0.05891
μ (10^{-4} kg/m•s)	5.8	6.4	0.09881	2.819
h_{fg} (kJ/kg)	112	93.1	217	2,257
C_p (kJ/kg•K)	1.18	1.04	0.7942	4.217
Dielectric Strength (kV, 0.1" gap)	40	38	N/A	N/A

2.2.2 Control Systems

Figure 2.6 and Figure 2.7 illustrate the control system, which consisted of a condenser connected by two tubes, called the inlet and outlet lines, to an external Neslab® RTE-7 Digital Plus water chiller. The setup allowed water to flow through the inlet tube into the condenser's copper coils that hang from the top copper plate inside the chamber. The water flowed out of the coils via the outlet line.

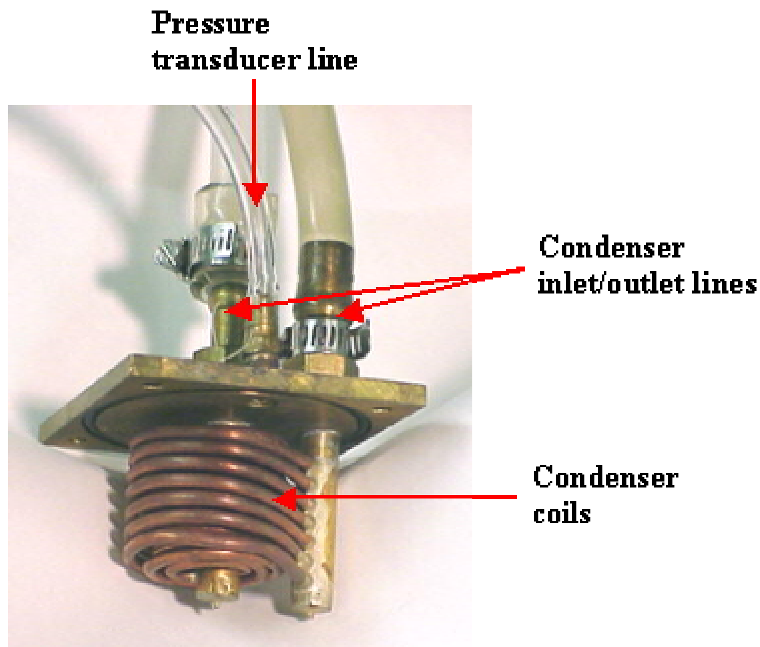

Figure 2.6: Side view of the condenser assembly.

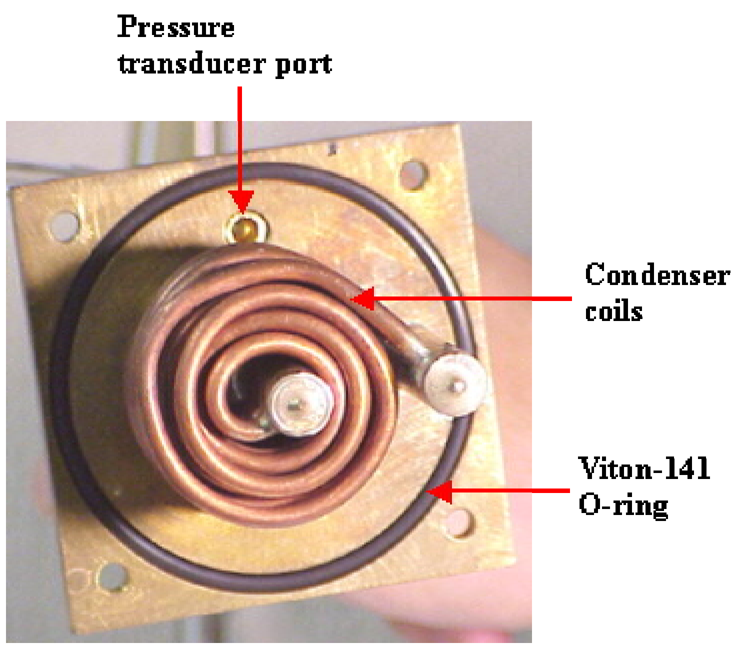

Figure 2.7: Bottom view of the condenser assembly.

2.2.3 Power Supply

A programmable DC power supply (Sorenson, Inc., model #DLM150-4M9G) provided power to the heater. The power supply was controlled by a data acquisition system (LabVIEW®) programmed on a personal computer through a general programming interface bus (GPIB) interface and DAS card.

2.2.4 Data Acquisition

Data was acquired through four thermocouples, a pressure transducer, a digital multimeter, a programmable power supply and LabVIEW®.

Temperature measurements were collected from four T-type thermocouples. Three of the thermocouples were produced and calibrated by Rinc, Inc; the fourth thermocouple probe was produced and calibrated by Omega Engineering™. The manufacturers' claimed accuracy for these thermocouples was ±0.1 °C. The three thermocouples produced by Rinc, Inc., were inserted into the thermocouple holes drilled in the heater referred to in section 2.2.1.2. The fourth thermocouple was placed in the chamber and immersed in the HFE-7100 fluid near the sample to measure the bulk temperature. A Setra pressure transducer measured the chamber pressure. The temperature and pressure readings were fed to an Agilent 34970A digital multimeter. This multimeter exported all data through a GPIB (general programming interface bus) interface to a PC. The Sorenson programmable power supply measured the power supplied to the heater. The readings were exported through the GPIB interface to LabVIEW®. Heat loss was negligible because the heater was well insulated and the nichrome plate provided poor thermal conductance in the radial direction. Therefore, the power reading exported to LabVIEW® did not require manipulation to determine the actual supplied power to the heater.

2.3 Experimental Procedure

Each sample was tested 4 or 5 times to ensure validity and reliability in the data collected. For each experiment, a clean test section and fresh HFE-7100 were used, and the test section was vacuumed to remove any gas from inside the chamber.

The chamber was heated to reach the appropriate testing conditions (60 ^{o}C and 1.0 atm). To avoid a negative heat flux traveling downwards (e.g. heat flux from the liquid to the heater), a small wattage of 10 – 15 W was supplied to the copper heater. The chiller was programmed to a temperature, which depended on the ambient temperature, maintaining the HFE-7100 environment at 1 atm. When the testing conditions were reached and the thermocouples were "stable" (see the next paragraph), data collection began.

LabVIEW® provided real time readings from the thermocouples, pressure transducer and programmable power supply. For each temperature reading, the average change in that reading over the preceding four minutes was calculated every 10 seconds. A measurement was considered stable when the average change in that measurement over the four-minute period was less than 0.1 ^{o}C at pressure between 0.997 and 1.004 atm and bulk fluid temperature between 59.6 and 59.8 ^{o}C. When the heater thermocouple temperatures, chamber pressure, and bulk fluid temperature became stable, LabVIEW® recorded the thermocouple readings, pressure reading, and supplied power. The recordings were then exported to Microsoft Excel®.

The power supplied to the heater was increased by roughly 5 W after the data was recorded for a specific data point. The measurement process described above was repeated at higher power levels. The supplied power was increased until either the sample reached critical heat flux (CHF) or the heater thermocouples reached 170 ^{o}C.

Temperatures above 170 ^{o}C were avoided because at 178 ^{o}C, the rosin solder would begin to melt, allowing the working fluid to force gaps between the nichrome surface and copper plate or finned microstructure. The gaps in the rosin solder would cause additional thermal resistance, leading to an inaccurate superheat reading. Furthermore, the hazardous decomposition limit of HFE-7100, which produces nerve gas, occurs at 200 ^{o}C. The CHF of copper foams was not reached because the wall temperature of CHF was above the set limit of 170 ^{o}C.

2.4 Data Analysis

The recordings collected were used in Microsoft Excel® to provide 10 to 15 data points to obtain a boiling curve similar to the one seen in Figure 2.8 for each sample of copper foam or copper-finned microstructure.

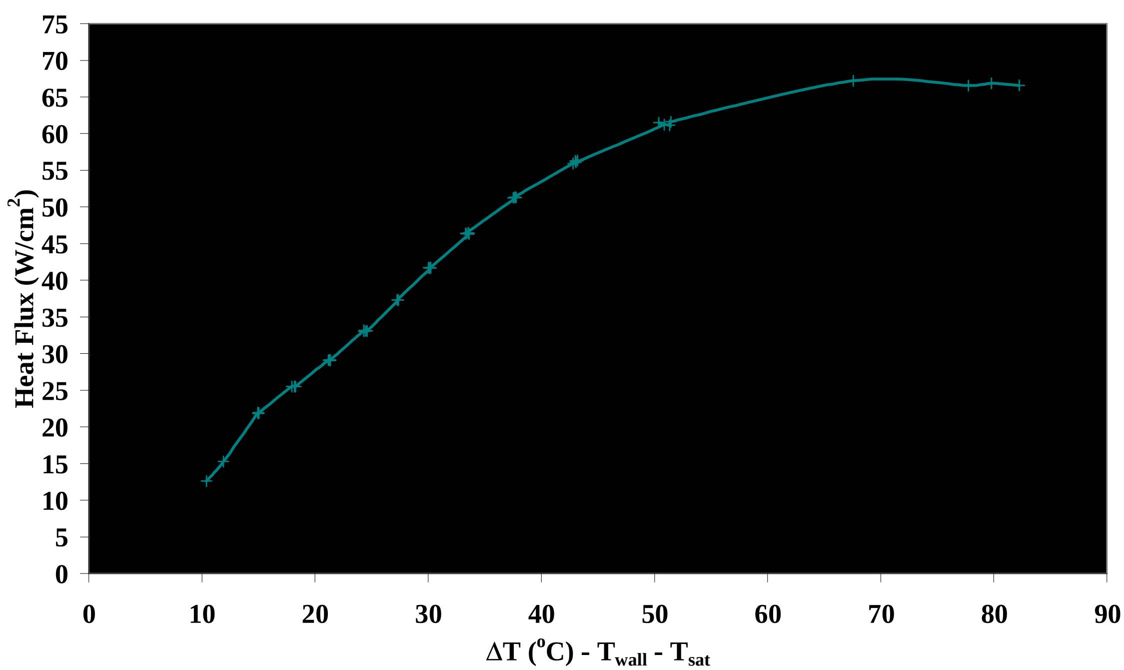

Figure 2.8: Typical boiling curve from obtained data points.

Each data point was calculated from the following values: the thermocouple readings (T_1, T_2, T_3,), bulk fluid temperature (T_{bulk}), pressure (P), supplied voltage (V), and supplied current (I). Figure 2.3 in section 2.2.1.2 illustrates the locations of the thermocouples.

The heater was well insulated by high-temperature engine paint and radial thermal conduction through the nichrome plate was minimal resulting in negligible heat loss. Therefore all supplied power by the Sorenson DC power supply was used strictly for heating the sample which means that heat flux was equal to the measured supplied power. The superheat (ΔT) was calculated as shown in Equation 2.1. Since the pressure was maintained at 1 atm throughout all of the experiments, T_{sat} (temperature of fluid based on the saturation pressure) was assumed to be the same as T_{bulk}.

$$T_{avg} = \frac{(T_1 + T_2 + T_3)}{3}$$

$$R_{cufoam} = \frac{L_{Cu}}{k_{Cu} \times A_{Cu}} + \frac{L_{nichrome}}{k_{nichrome} \times A_{nichrome}} + \frac{L_{solder}}{k_{solder} \times A_{solder}} + \frac{L_{CuPlate}}{k_{CuPlate} \times A_{CuPlate}}$$

$$R_{CuFins} = \frac{L_{Cu}}{k_{Cu} \times A_{Cu}} + \frac{L_{nichrome}}{k_{nichrome} \times A_{nichrome}} + \frac{L_{solder}}{k_{solder} \times A_{solder}} \tag{2.1}$$

$$T_{surface} = T_{avg} - q \times R$$

$$\Delta T = T_{surface} - T_{sat}$$

2.5 Error Analysis

The calculation of errors in all measurements taken was based on information provided by Rinc Inc., Omega Inc., Agilent, Sorensen, and Mitutoyo, the manufacturers of the measuring equipment. The thermocouples were calibrated in distilled ice and boiling water, providing an error of ±0.1 ºC. The multimeter had an error of ±1.0 ºC causing the total temperature measurements to have an error up to ±1.1 ºC. The standard deviations of the thermal conductivity varied based on the temperature, making it necessary to calculate the standard deviation of the heat flux for each steady-state point. The voltage and current measured by the power supply had an error of ± (0.1% + 0.15%FS) and ± (0.1% + 0.4%FS), respectively. The calipers, manufactured by Mitutoyo and used to measure the volume of the samples had an error of ±0.02 mm. Furthermore, a contact resistance existed in the solder layer where HFE-7100 may have been able to enter. It was assumed that 15% of the layer was a conservative amount between the nichrome plate and copper plate that was filled with HFE-7100. Also, it was assumed a contact resistance was located between the copper heating block and the nichrome plate and between the copper base plate and the copper foam, allowing the total resistance to increase from 0.106509 K/W (includes no contact resistance) to 0.110271 K/W. The contact resistance was negligible because it increased the total thermal resistance 3.53% higher than the ideal case (no contact resistances). Based on these errors, standard deviations in the heat flux results were calculated as shown in Equation 2.2. The standard deviations in wall superheat were calculated as shown in Equation 2.3.

$$dq = \sqrt{\left(\frac{I}{A}dV\right)^2 + \left(\frac{V}{A}dI\right)^2 + \left(\frac{IV}{A^2}dA\right)^2} \qquad (2.2)$$

$$d\Delta T = \sqrt{dT_{wall}^2 + dT_{bulk}^2} \qquad (2.3)$$

In particular, some errors were found to be as follows:

- The standard deviation in the heat flux in low heat input regions was ±2.8%.
- The standard deviation in the heat flux in high heat input regions was ±1.2%.
- The standard deviation in the wall superheat in all heat inputs was ±1.56ºC.

Heat loss through the nichrome plate was calculated using Equations 2.4 and 2.5. It was approximately 3% more than the assumed amount of heat loss (assumed heat loss was 2%). This additional heat loss amount was used with the heat flux error from the measurement devices in a sum of squares method to determine a total heat flux error of 3%. Heat loss from the nichrome plate was neglected because the maximum heat flux error was insignificant relative to the 2.8% equipment error.

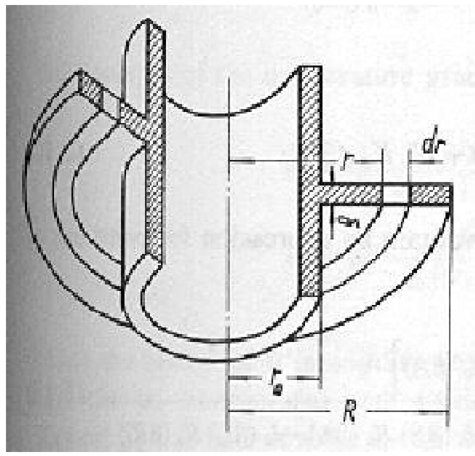

Figure 2.9: Dimensions used for heat loss through nichrome plate (Stasiulevicius, 1988).

$$Ra_L = \frac{g\beta(T_{base} - T_{bulk})L^3}{\nu\alpha}$$
$$Nu_L = 0.15 Ra_L^{1/4}$$
$$h_L = \frac{Nu_L k_l}{L} \qquad \text{(2.4, Incropera, et al., 2001)}$$
$$L = \frac{A_s}{P_1 + P_2}$$
$$\beta = \frac{1}{T_{base}}$$

$$Q_{loss} = k_{nichrome} f_0 \beta \vartheta_1 \psi'$$
$$f_0 = 2\pi R_1 \delta$$
$$\beta = \sqrt{\frac{2h_L}{k_{nichrome}\delta}} \qquad \text{(2.5, Stasiulevicius, et al., 1988)}$$
$$\vartheta 1 = T_{base} - T_{bulk}$$
$$\psi' = \frac{I_1(\beta R_2)K_1(\beta R_1) - I_1(\beta R_1)K_0(\beta R_2)}{I_0(\beta R_1)K_1(\beta R_2) + I_1(\beta R_2)K_0(\beta R_1)}$$

2.6 Summary

Samples in this study were evaluated by their rate of thermal performance. A specially designed apparatus was built to ensure that all testing conditions remained constant for all samples. This section describes in detail the testing apparatus and experimental procedure. When the values of T_1, T_2, T_3, T_{bulk}, I, V, and P of each sample were collected, a series of mathematical calculations was performed to obtain superheat values. Errors in superheat and heat flux were also calculated. Superheat, heat flux and their errors were plotted on boiling curves to evaluate each sample's thermal performance.

3. RESULTS FOR POOL BOILING ON COPPER FOAMS

3.1 Introduction

This chapter presents results for thermal performance characteristics of copper foams and their comparison with base case pool boiling data. Pool boiling curves were obtained with various copper foams bonded to the heated surface. The foam parameters that were varied included pore density, foam thickness and porosity. The porosity was determined by the ratio of pore volume to total volume as illustrated in the following Equation 3.1.

$$\begin{aligned} \xi &= \frac{\left(m_{copperblock} - m_{foam}\right)}{m_{copperblock}} \\ m_{copperblock} &= Volume \times \rho_{copper} \\ m_{foam} &= measured \end{aligned} \tag{3.1}$$

The first part of this chapter discusses the base case data and is followed by an exposition of the data for copper foams investigated in the present study. Comparison of the base case data with the copper foam data established the performance gain associated with the copper foams.

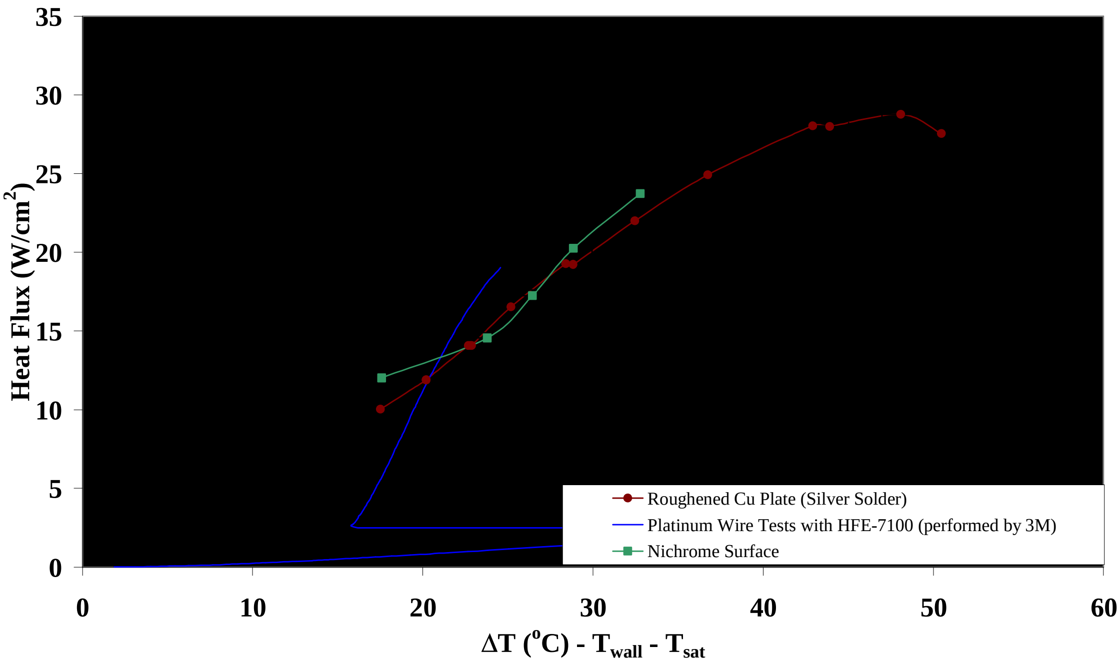

Figure 3.1: Results of base tests with a nichrome and scratched copper surface, and a platinum wire.

Tests were performed on the flat nichrome surface and a scratched copper plate (bonded with silver bearing solder) under the test conditions (1 atm, 60 ^{o}C). In order to determine the thermal performance of the copper foams, base line tests were necessary. The scratched copper plate was polished with 320-grit sandpaper creating small cavities on the top surface of the copper plate. 3M^{TM} provided pool boiling data for a 4.75 cm platinum wire with diameter 0.05 cm in HFE-7100 which allowed its thermal performance to be plotted with the thermal performance of the nichrome plate and scratched copper plate, providing base line tests.

The thermal performance for the scratched copper plate and the nichrome plate are similar to those shown in Figure 3.1. CHF occurred at a higher wall temperature for the scratched copper plate because the scratched plate's cavities allowed more liquid to contact the surface at high superheats through thermocapillary effects. Thermal performances of a scratched copper plate and nichrome plate were plotted with the given platinum wire data to establish a benchmark for the comparison of thermal performances of the copper foams and copper-finned microstructures.

3.2 Effect of Pore Density

Two sets of samples were tested to evaluate the effect of pore density on copper foams. The first samples tested had varying pore density with thickness 2 mm and porosity 0.92. The second samples tested had thickness 5 mm with porosity 0.93. Results for the first test samples are shown in Figure 3.2. An increase in pore density enhanced the thermal performance of the copper foam sample for the range of parameters tested.

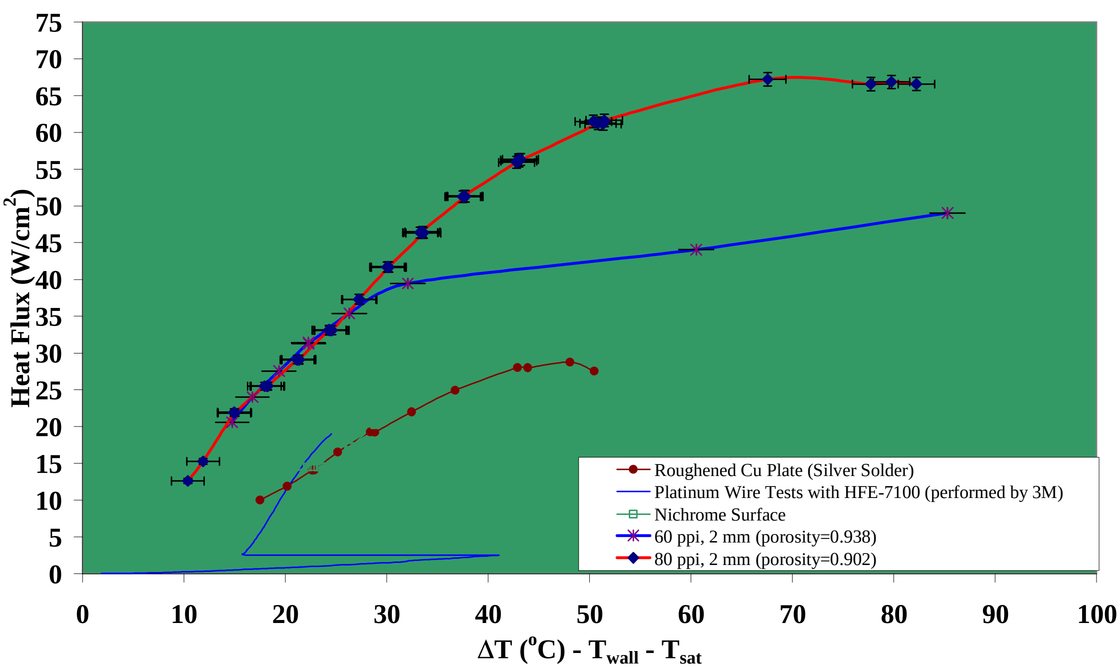

Figure 3.2: Boiling curves demonstrating the effect of pore density at 2 mm thick.

The effect of pore density was also investigated for foams of thickness 5 mm. Thermal performance increased with pore density until the pore density reached 45 PPI as seen in Figure 3.3. For pore densities greater than 45 PPI, however, thermal performance decreased. For 5 mm thick foams, there was an optimal value for pore density close to 45 PPI. Increased pore density beyond the optimal value (with constant porosity) yields more copper ligaments and further limits the pore sizes. Therefore, vapor bubbles are prevented from escaping and as a result thermal performance decreases as pore density increases beyond the optimal value.

The results of the effect of pore density agree with Ramaswamy et al.'s (2003) conclusion, in that thermal performance increases with increasing pore density. The results do not support his statement once the pore density is increased beyond an optimal value at increased thicknesses tested in this study.

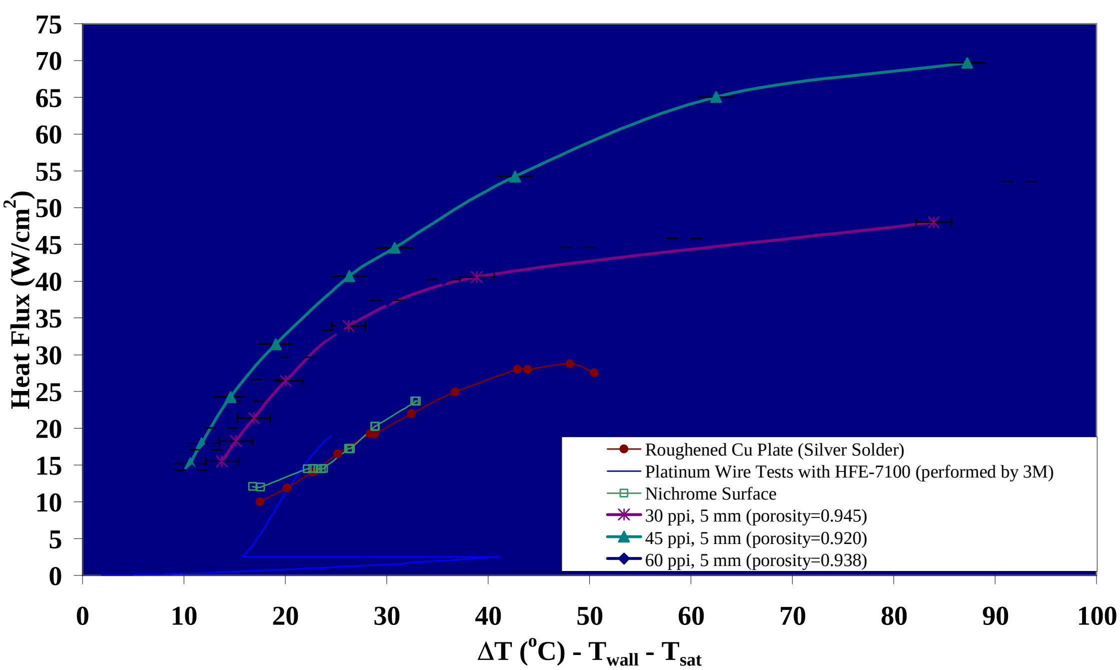

Figure 3.3: Boiling curves demonstrating the effect of pore density at 5 mm thick.

3.3 Effect of Thickness

Experiments were conducted on 45 PPI and 60 PPI foam samples with varying thicknesses. Results are depicted in Figure 3.4 and Figure 3.5.

Increased thickness enhanced the thermal performance of copper foam as seen in Figure 3.4 for the 45 PPI foam samples. However, the increasing thickness of the copper foam resulted in a change in porosity. Two variables (thickness and porosity) were changing negating the accuracy of the test. It was necessary to further investigate how thickness affected the heat flux when porosity was constant.

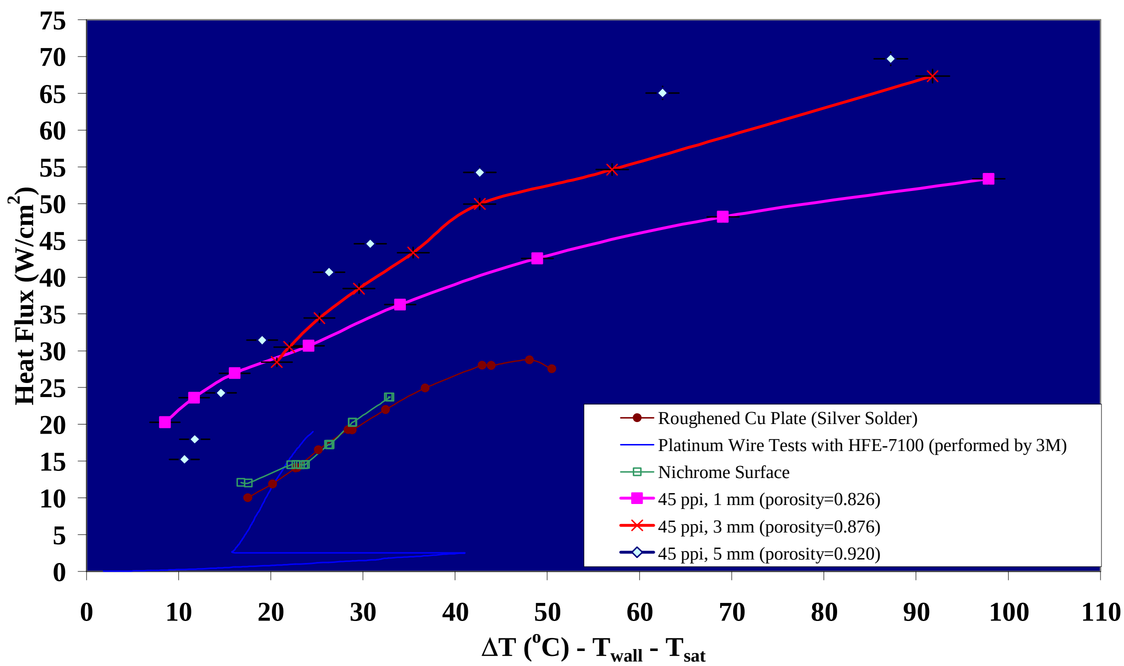

Figure 3.4: Boiling curves demonstrating the effect of thickness at 45 PPI.

Tests were performed next on foams of pore density 60 PPI and porosity 0.938 with thicknesses of 2 and 5 mm. As shown in Figure 3.5 below, thickness moderately influences thermal performance at high superheats, but does not affect the thermal performance at low and intermediate superheats. The data only supports Ramaswamy et al.'s (2003) statement that thermal performance increases with increased thickness at high superheats. The experimental data does not support Ramaswamy et al.'s theory that decreased thickness at low superheat leads to increased thermal performance. The data does not support Coursey's (2003) statement that increased thickness inhibits thermal performance. The discrepancy between data from this study and data in Coursey's (2003) study could be attributed to the fact that the copper foams and the bonding used in this present study were different from the graphite foams of Coursey's study. The data does support Athreya et al.'s (2002) hypothesis that with increased thickness there is increased thermal performance. The data does not support his statement that an intermediate thickness exhibits the lowest thermal performance. This difference could be attributed to the fact that the data collected from the present study was from copper foams with pore density of at least 30 PPI while Athreya et al.'s data was collected from aluminum foams at lower pore densities values (around 5 PPI). More importantly, the data shows that foam thickness barely affects thermal performance for these dense copper foams (30 PPI or higher). Therefore, porosity is the dominant parameter affecting thermal performance for high foam densities (30 PPI or higher).

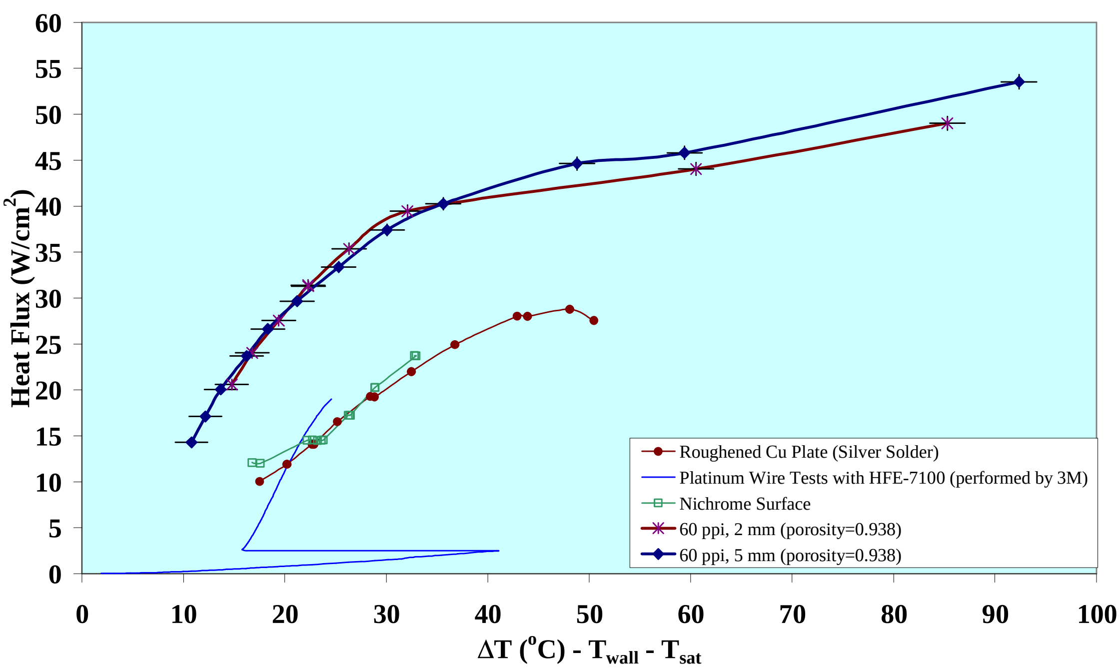

Figure 3.5: Boiling curves demonstrating the effect of thickness at 60 PPI.

3.4 Effect of Porosity

Tests in this study were conducted on copper foams of constant pore density and thickness to evaluate the effect of porosity on thermal performance. Test results performed on foams of 60 PPI and 2 mm foams are shown in Figure 3.6. The figure shows that thermal performance increased as the porosity increased from 0.779 to 0.854, but with further increase in porosity to 0.938, the thermal performance decreased. This suggests that for a given foam thickness, pore density, and foam type, there is an optimum porosity for which the thermal performance is maximum. It should be noted that as the porosity approaches 1, the foam ligament volume decreases, causing the foam to act more like a smooth surface, losing its micro structured-induced augmented boiling.

The above-referenced finding on the effect of porosity agrees with Ramaswamy et al.'s (2003) conclusion that thermal performance increases with increasing porosity. However, Ramaswamy et al.'s results did not extend to higher porosities approaching 1. Ramaswamy et al. did not identify the fact that beyond an optimum value further increase in porosity may not help the thermal performance of a given foam. Moreover, unlike Ramaswamy et al.'s results for microfabricated silicon evaporators where thermal performance increased with increasing porosity only at low and intermediate superheat, the results obtained in the present study suggest that at high superheats, thermal performance is enhanced with increasing porosity.

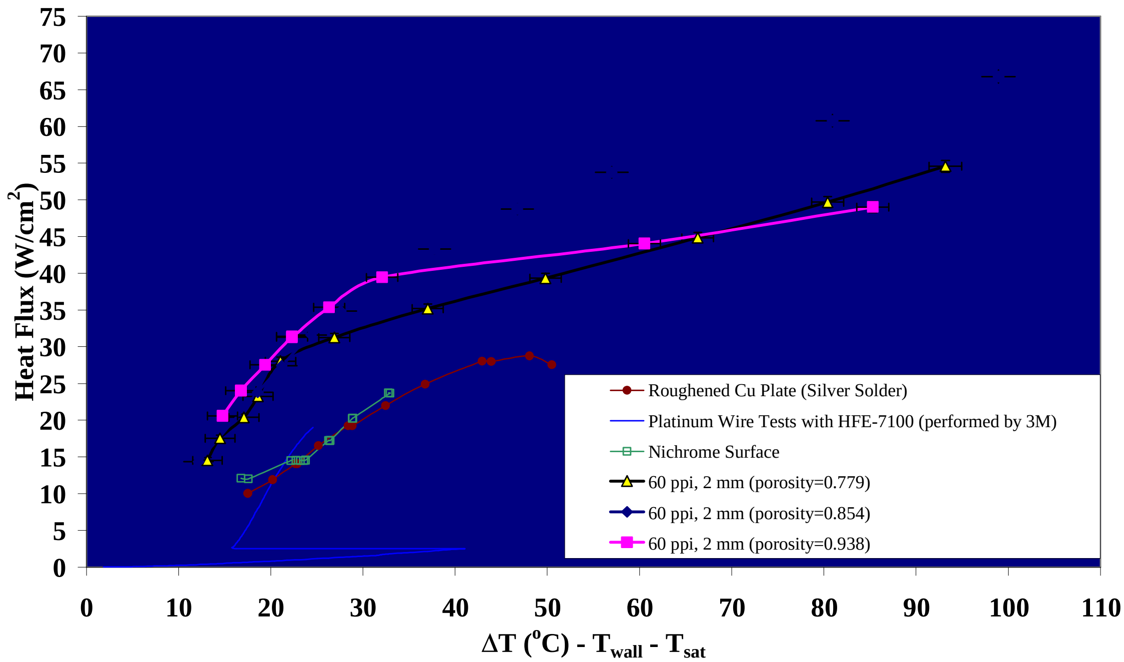

Figure 3.6: Boiling curves demonstrating the effect of porosity at 60 PPI and 2 mm thick.

3.5 Dynamics of Pool Boiling in Copper Foams

It is necessary to determine how boiling occurs in the interior of the foam to better understand how heat is dissipated from the foam. Viewing the bubble interaction within the foam without affecting the foam's thermal performance is difficult. Therefore analysis must be performed by other means. As an alternative, the resistance of the fluid flow caused by the ligaments as well as the temperature distribution within the foam were determined by dimensionless analysis and a fin effect, respectively. Dimensionless analysis determined the dominant force involved (surface tension, viscous force and buoyancy force) in the foam. The fin effect considered the boiling only occuring on the outside surfaces of the foam. Analysis of these parameters are discussed briefly in the following sections:

3.5.1 Resistance Due to Ligaments

The main deterrent of heat transfer was determined using the Bond, Capillary and Grashof dimensionless numbers as shown in the following equations. The Bond number is the ratio of buoyancy force to surface tension force, the Capillary number is the ratio of viscous force to surface tension force, and the Grashof number is the ratio of buoyancy force to viscous force.

$$Bo = \frac{g(\rho_l - \rho_v)d_{pore}^2}{\sigma} \tag{3.2}$$

$$Ca = \frac{We}{Re} = \frac{\mu u}{\sigma} \tag{3.3}$$

$$Gr = \frac{g\beta(T_{wall} - T_{sat})d_{pore}^3}{\nu^2} \tag{3.4}$$

The Capillary number depends on the velocity of the fluid and the Grashof number is dependent upon the superheat making it necessary to first determine the liquid velocity and superheat. Data from a 60 PPI, 2mm copper foam with a porosity of 0.854 was used to find these values. It was assumed that latent heat transfer was the primary mechanism of heat transfer because convection currents other than latent heat transfer would be impeded by thermal equilibrium between the solid and fluid as stated by Wong et al. (1976). The estimated mass flux by heat transferred from the foam can be expressed as

$$q = \dot{m}h_{fg} \tag{3.5}$$

The mass flow rate is given by Equation 3.6 below (the product of fluid velocity, fluid density and cross-sectional area) for vapor and liquid.

$$\dot{m} = u_{v,l}\,\rho_{v,l}\,A_c \qquad (3.6)$$

The velocity can then be calculated as a function of the heat flux, density, and latent heat as shown below.

$$u_{v,l} = \frac{q}{\rho_{v,l}\,A_c\,h_{fg}} \qquad (3.7)$$

For the 60 PPI, 2mm thick copper foam sample with porosity 0.854, the heat dissipation was 66.8 W, the superheat was 66.8 ^{o}C and the cross-sectional area was 1 cm^2. The vapor and liquid velocities were calculated to be 62.66 m/s and 0.436 m/s, respectively. The three dimensionless numbers (Bond, capillary, and Grashof number) were then calculated using the above determined velocities and the superheat, resulting in a Bond number of 0.11, Capillary number of 0.024, and Grashof number of 410. Table 3.1 shows Bond, capillary, and Grashof numbers for all the copper foam samples tested. Buoyancy forces and surface tension forces controlled the heat transfer more than liquid viscosity because the Grashof and Bond number were significantly higher than the Capillary number for foams tested in the present study. It is known that when the Bond number is lower than 1, buoyancy force is lower than the forces caused by surface tension. For these experiments heat transfer is predominately controlled by surface tension reducing bubble departure frequency in the copper foam structures.

Table 3.1: Bond, capillary, and Grashof numbers for each copper foam sample.

PPI and thickness	Porosity	Average Pore Diameter (cm)	Bond Number	Capillary Number	Grashof Number
30 PPI, 5 mm	0.945	0.082	0.86	0.017	7,673
45 PPI, 1 mm	0.826	0.030	0.12	0.019	463
45 PPI, 3 mm	0.876	0.045	0.26	0.024	1451
45 PPI, 5 mm	0.920	0.054	0.38	0.025	2310
60 PPI, 2 mm	0.779	0.028	0.10	0.020	351
60 PPI, 2 mm	0.854	0.029	0.11	0.024	410
60 PPI, 2 mm	0.938	0.030	0.12	0.018	387

PPI and thickness	Porosity	Average Pore Diameter (cm)	Bond Number	Capillary Number	Grashof Number
60 PPI, 5 mm	0.938	0.030	0.12	0.019	387
80 PPI, 2 mm	0.902	0.022	0.06	0.024	152
100 PPI, 1 mm	0.846	0.014	0.03	0.023	26

3.5.2 Fin Effect Model

The foam was modeled as a fin with heat transfer occurring on the top and 4 vertical sides of the foam to evaluate the heat transfer from the foam. As a result, heat flux was decreased. Lowered heat flux from foams is common in surface tension controlled porous media. The thermal performance can be determined by using the local convection heat transfer as expressed in the following equation:

$$q_x'' = h_x \left(T_x - T_\infty\right) \tag{3.8}$$

The local heat transfer coefficient (h_x) in Equation 3.8 varied from point to point within the foam, as determined by the local superheat and containment of the pores. The local heat transfer was difficult to explicitly determine locally. Wong et al. (1976) stated that there is a negligible temperature difference between the solid and fluid phases inside the porous media. Assuming this, negligible convection heat transfer occurs within the foam, allowing only latent heat transfer to dominate. A small mass flux exists due to the presence of high surface tension, eliminating the latent heat transfer.

By assuming latent and convection heat transfer within the foam was negligible, the foam was modeled as a solid block with heat transfer only occurring through boiling on the outside surfaces. In Coursey's (2003) numerical simulation, he concluded that surface temperature was almost constant throughout the foam, suggesting a single average heat transfer rate throughout the foam. Following Coursey's reasoning, the heat transfer coefficient was calculated using the 60 PPI, 2 mm thick copper foam with a porosity of 0.854. This foam had an outer surface area of 1.8 cm^2, an average superheat of 43.25 ^{o}C, and total steady-state heat flux of 66.8 W. The average heat transfer coefficient on all of the outer surfaces was calculated to be 8,579 W/(m^2·K). According to the data from the boiling curve in Figure 3.6, the heat transfer coefficient was as much as 8,111 W/(m^2·K) given an average superheat of 14.4 ^{o}C. The heat transfer coefficients agree with typical boiling heat transfer coefficients reported in Coursey's findings, as opposed to those predicted from calculations involving the total surface area inside and outside of the foam because the calculated heat transfer coefficients based on Equation 3.8 are above 2,500 W/(m^2·K). The boiling curve in Figure 3.7 was constructed to demonstrate the heat flux from the outer surfaces of the foam (surface area that includes the top and side surfaces) with the supplied power and superheats of Figure 3.6. Comparison of the results in both figures further illustrates the point that the lower thermal performance from the foam's outer surfaces is caused by surface tension controlled boiling.

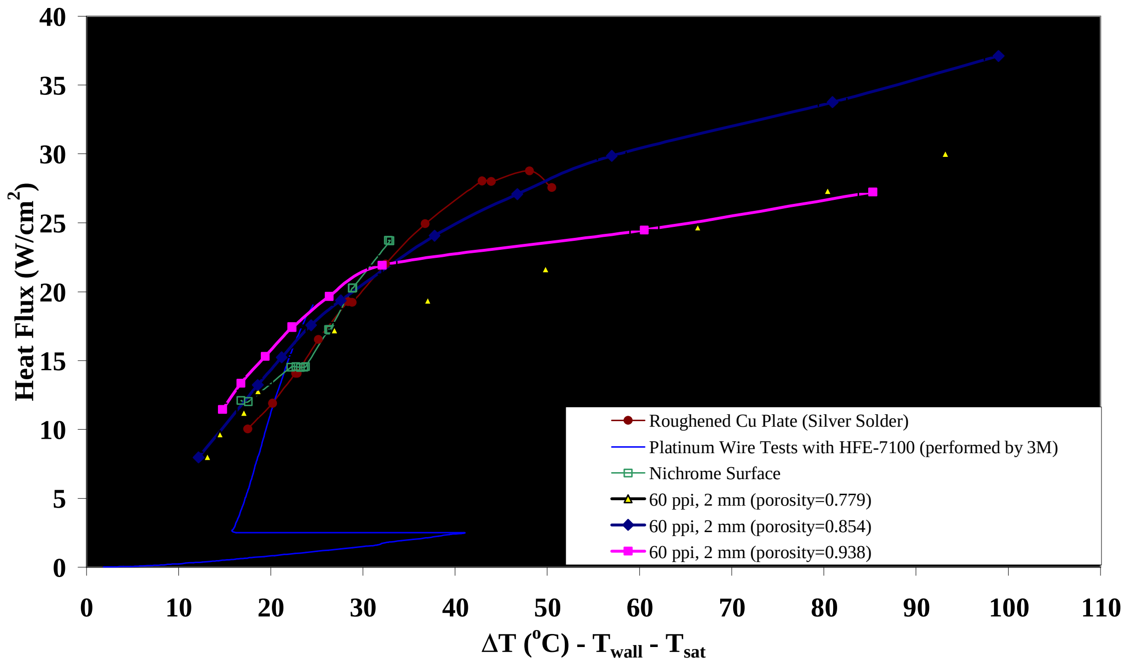

Figure 3.7: Boiling curves demonstrating heat transfer from the outer surfaces of the 60 PPI, 2mm copper foams.

3.6 Summary of Results for Pool Boiling on Copper Foams

The thermal performance of various copper foams were studied was studied through a series of experiments. Foams studied had different pore density, thickness and porosity. Through dimensionless analysis, the effects of viscous forces, surface tension, and buoyancy forces on the thermal performance through boiling within the foam were investigated. The main conclusions are as follows:

This research study showed that at high pore densities, thickness did not affect the thermal performance of copper foams. At low pore densities (45 PPI), a higher thickness performed better so long as their porosity was optimized. It is critical to design foam with correct pore sizes to ensure optimal thermal performance. The pore size of a foam is determined by the pore density and porosity. The ligament volume determines porosity.

Therefore, pore density and porosity are the most important parameters in thermal performance of the foams studied.

Surface tension within the foam served as the main deterrent for bubbles to depart from the surface. Through dimensionless analysis, it was found that surface tension force is roughly 10 times the size of the buoyancy force and that viscous forces are negligible. Thermal performance is reduced as a result of small pore sizes preventing bubbles from escaping. Under such conditions the boiling process of the copper foam was modeled as a solid block with heat transfer only taking place on the outer surface of the foam. The results support Coursey's (2003) findings, which stated that boiling only occurs on outside surfaces and vapor is the only phase of the working fluid existing within the foam. Depending on the superheat, the average heat transfer coefficient for boiling HFE-7100 from a copper foam surface ranged from 2,000 to 9,000 W/(m^2·K). However, the average heat transfer coefficient for removing heat loads from the 1 cm^2 footprint via copper foams ranged from 5,100 to 15,000 W/(m^2·K).

The thermal performance of copper foams was greater than the thermal performance of the base line tests. The copper foams had a thermal performance ranging between 10 and 75 W/cm^2 for a superheat range of 10 to 100 ^oC. Meanwhile, the thermal performance of the nichrome plate ranged between 12 and 24 W/cm^2 for a superheat range of 17 ^oC to 27 ^oC.

4. RESULTS FOR POOL BOILING ON COPPER MICRO-FINNED SURFACES

4.1 Introduction

The second set of enhance surfaces tested in the current study involved surfaces with microgrooves on the surface. The grooves provided additional surface area while at the same time they promoted nucleation boiling on the surface by creating additional cavities as nucleation sites. These surfaces were manufactured by Wolverine Tube, Inc.™ (a leading manufacturer of enhanced boiling and condensation heat transfer tubes in the U.S. and internationally, headquartered in Decatur, AL). Figure 4.1 schematically depicts the geometric structure of these surfaces. A photographic view of these surfaces is shown in Figure 4.2. Although due to the proprietary nature of these surfaces, detailed manufacturing of the surface is not known to us, it appears the technology is an expansion of what is being used at Wolverine Tube, Inc.™ to fabricate enhanced boiling surfaces. The parameters that characterize micro-finned surfaces are shown in Figure 4.1. They include fin density and aspect ratio. The aspect ratio is the ratio of channel height to channel width. With limited samples available in the present study, the effect of fin density and aspect ratio were addressed.

When compared to copper foams, micro-finned surfaces require significantly less thickness and volume, thus are preferred for applications such as avionics and aerospace applications where component as well as system-level savings in weight/volume requirements are very critical. On average, the typical copper-finned microstructure volume (0.06 cm^3) is only 18% of the corresponding copper foams' average volume (0.32 cm^3).

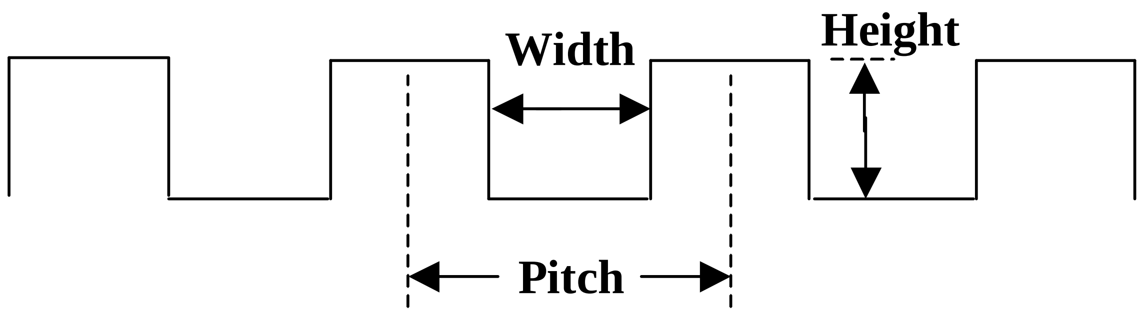

Figure 4.1: Schematic of copper-finned microstructures.

$$
\begin{aligned}
&\text{FPI (fins per inch)} = n/L \\
&L = n\,(P - w) + w\,(n - 1) \\
&\therefore P = (L + w)/n \\
&t = P - w = \text{fin thickness} \qquad\qquad (4.1) \\
&P = \text{pitch} \\
&w = \text{channel width} \\
&L = \text{length along the horizontal side} \\
&n = \text{number of fins} \\
&\text{aspect ratio} = h/w \\
&h = \text{fin height}
\end{aligned}
$$

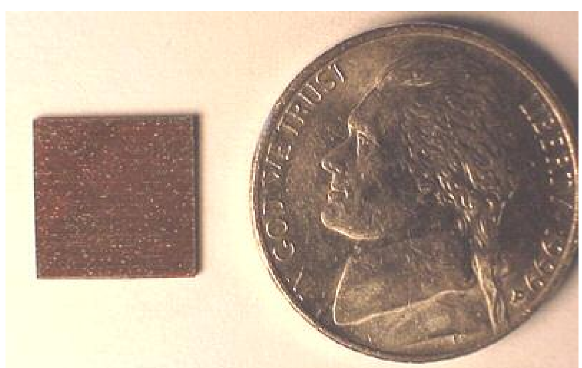

Figure 4.2: Photograph of a copper-finned microstructure.

Eight Wolverine Tube, Inc.™ copper-finned microstructures were tested in the present study. Three of the samples tested had identical fin density and channel width, but varying aspect ratio (ratio of channel height to channel width). Three other samples with a constant aspect ratio but varying fin density were tested.

4.2 Effect of Changing Aspect Ratios

Three copper-finned microstructures with 212 FPI, 0.0584 cm channel width, and heights of 0.51 cm, 0.58 cm and 1.27 cm (aspect ratios of 9, 10 and 22, respectively) were tested. The channel cross-section size was the only variable parameter. Figure 4.3 illustrates that thermal performance is enhanced at higher aspect ratios. A higher aspect ratio provides more surface area for a given channel width, thus a higher heat removal capacity at a lower superheat is obtained. The boiling curves of samples #6 and #7 are within each other's error regime that they essentially provide the same thermal performance.

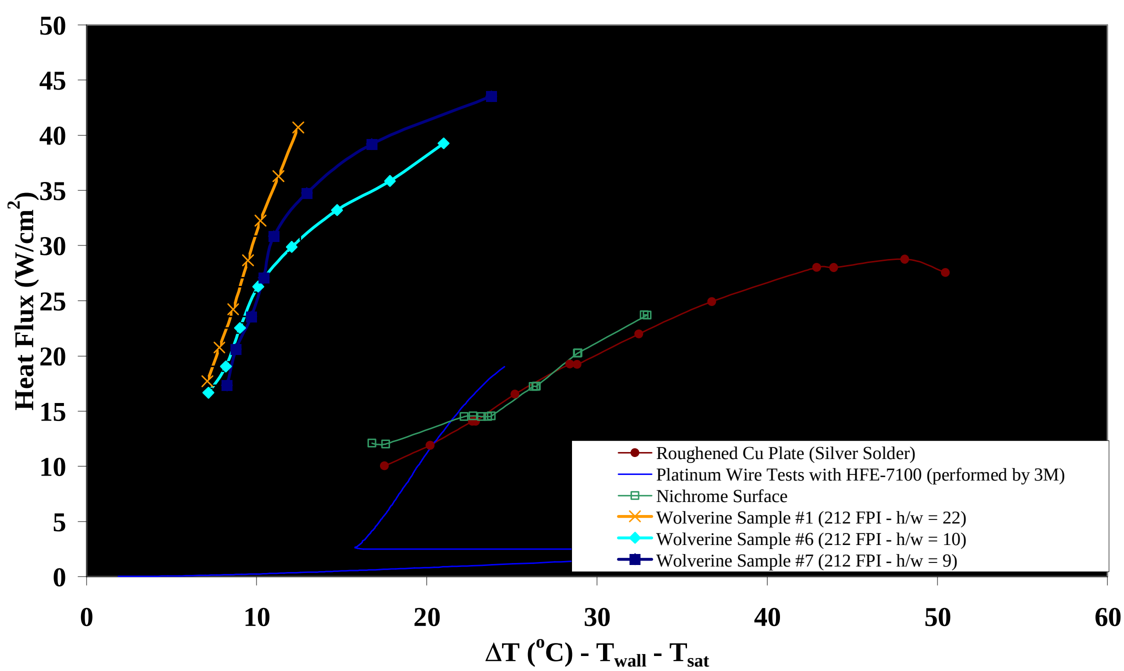

Figure 4.3: Boiling curves demonstrating the effect of aspect ratio.

4.3 Effect of Fin Density

Effect of fin density on thermal characteristics of the micro-finned surfaces was examined next. Tests were conducted on copper-finned microstructures of fin densities 185, 212, and 212 FPI with aspect ratios of 9, 9, and 10, respectively. The results of fin density effect are shown in Figure 4.4. As seen there, enhanced thermal performance occurred with decreasing fin density. This occurred because at reduced fin density, for a given aspect ratio, a larger channel width and channel height is available with a larger surface area, thus higher heat fluxes can be achieved. Therefore, for the limited range of parameters tested, it appears that lower fin density and increased aspect ratios yield higher heat transfer rates. The boiling curves of samples #6 and #7 are within each other's error regime that they essentially provide the same thermal performance.

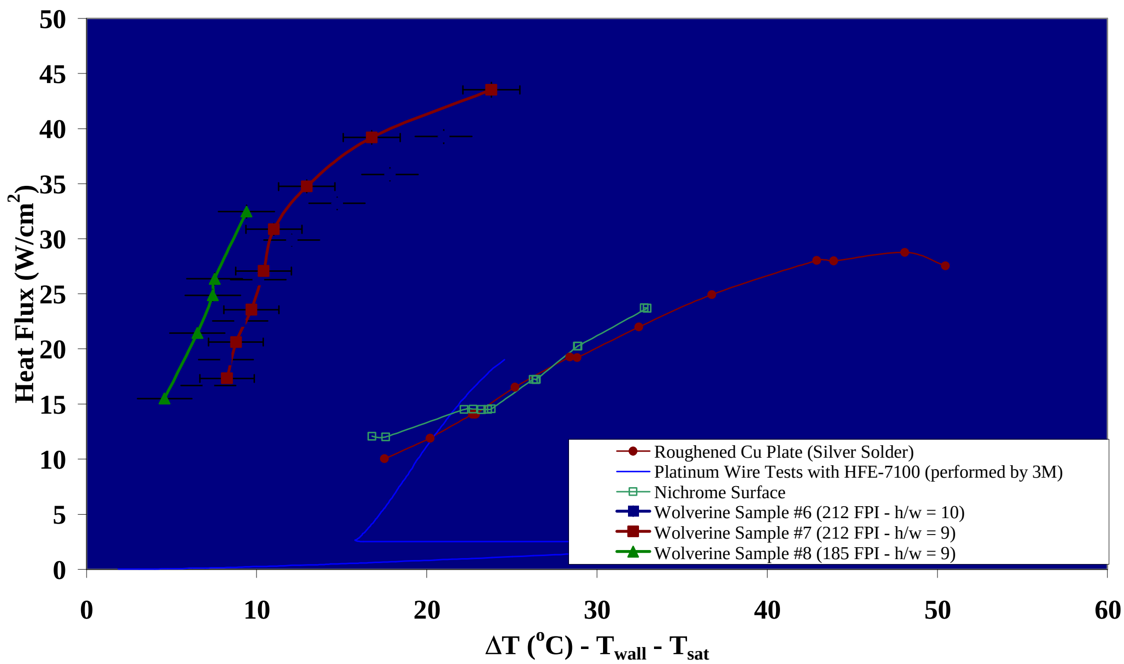

Figure 4.4: Boiling curves demonstrating the effect of fin density.

4.4 Comparison with Copper Foams

The data from all micro-finned surfaces and copper foams are brought together in Figure 4.5. From the data it can be deduced that the average heat transfer coefficient for boiling HFE-7100 using a copper-finned microstructure was 15,500 – 28,000 W/(m^2·K), greater than the 5,100 – 15,000 W/(m^2·K) average heat transfer coefficient for the copper foams tested. The average heat transfer coefficients were calculated by the maximum heat flux, average superheat, and outside surface area (not including channel surface area) of each sample as seen in Equation 4.2. The CHF of the copper-finned microstructures occurred at a lower heat flux than that of the foam. However, the superheat is less than that of the foams. As discussed earlier, an ideal boiling surface for electronic cooling applications will be the one that gives high heat fluxes at a minimum superheat. Therefore, additional optimization of the copper-finned microstructures is necessary to further improve thermal performance of these surfaces.

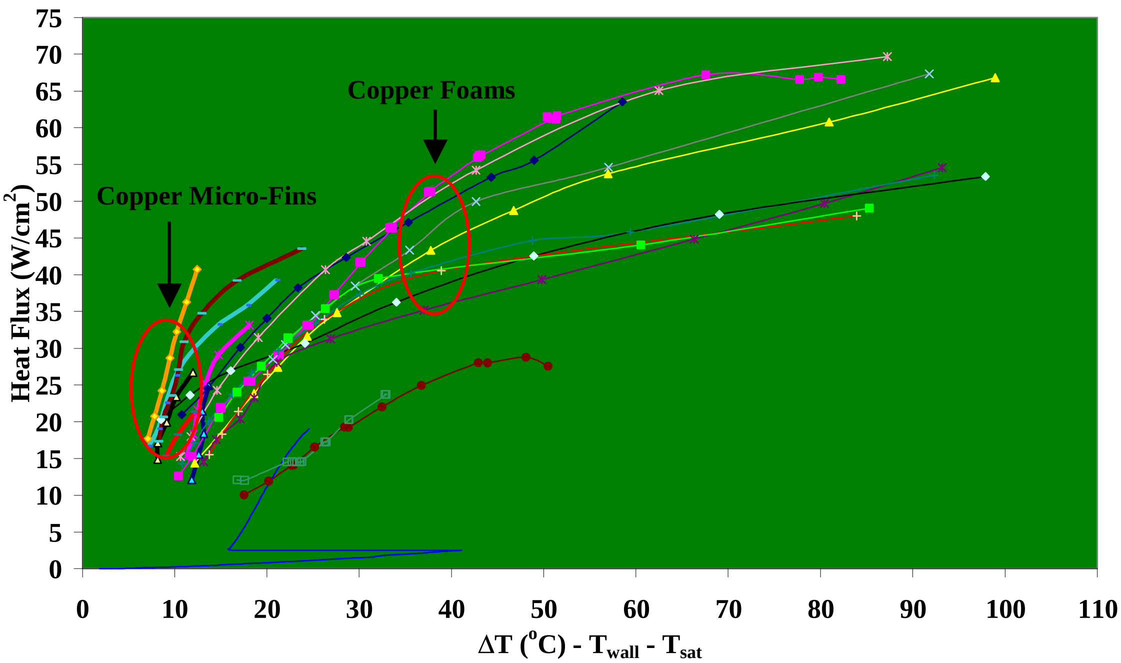

Figure 4.5: Boiling curves for all copper foams and copper-finned microstructures tested.

$$h_{avg} = Q_{max}/(A_{outside} \times \Delta T_{avg}) \qquad (4.2)$$

A realistic comparison of the copper foam with micro-finned surfaces will have to involve fabrication cost and reliability. Although details have not been provided to us by the manufacturer, it is our understanding that fabrication costs of micro-finned structures is comparable to those of copper foams if we take into account the bonding procedure required for each structure. Both surfaces offer substantially lower costs than their respective graphite or other foam structures.

4.5 Summary of Results for Pool Boiling on Copper-finned Microstructures

Experiments measuring thermal performance characterization of copper-finned microstructures with various fin densities and aspect ratios were performed as part of the present research study. The thermal performance of the copper-finned microstructures was substantially better than the smooth (base line) surfaces.

Channel hydraulic diameter is one of the key parameters in a successful design of the copper-finned microstructure boiling heat transfer surface. Another important factor is the fin density, or fins per inch. Copper-finned microstructures with a larger channel size allow for increased cooling. Copper-finned microstructures with lower fin densities yield increased thermal performance because the channel size is greater at lower fin densities. A higher aspect ratio with a constant fin density causes an enhanced thermal performance. An optimum fin density provides the maximum heat transfer coefficient for a given hydraulic diameter. The copper-finned microstructures displayed thermal performances between 20 and 45 W/cm^2 at 10 ^{o}C superheat. This corresponded to a heat flux rate of approximately 13 W/cm^2 at 10 ^{o}C superheat for the copper foams. Comparatively, the nichrome plate had a heat transfer rate of approximately 5 W/cm^2 at 10 ^{o}C superheat, thus verifying much less performance when compared to foams and micro-finned surfaces. On average, for the range of parameters tested the copper-finned microstructures' thermal performance was approximately 1.5 fold greater than the copper foam’s thermal performance and 4 fold greater than the nichrome plate’s thermal performance.

5. CONCLUSIONS AND FUTURE WORK RECOMMENDATIONS

This thesis presented results of an experimental investigation on thermal system characterization of selected copper foams and micro-fin structured boiling surfaces. The main distinction between these surfaces and other foams, such as graphite foams is the present samples production cost is supposed to be roughly an order of magnitude less than the corresponding graphite foams. The most significant findings of this research included the following:

1) When compared to smooth surfaces both microstructures substantially outperform the boiling on a smooth surface.

2) Increasing pore density and lowering thickness of the copper foams within the range tested (60 and 80 PPI, 2 mm) yields enhanced thermal performance at high superheats (e.g. more than 25 ^{o}C in this case).

3) For the range of parameters tested here, foam thickness of less than 5 mm does not seem to affect the thermal performance.

4) Porosity (a measure of open volume on the foam) and pore density (number of pores per inch) are the two most important properties of a given foam, as they greatly affect the typical thermal characteristics of a foam.

5) Experimental evidence suggests that surface tension force is about 10 times greater than the buoyancy force in the copper foams tested here. Moreover, the viscous forces in copper foams are negligible. As a result, heat transfer is reduced when pore sizes of the foam become too small, due to vapor bubbles prevented from escaping from within the foam. As pore size increases, the surface tension has less of an effect on the vapor bubbles.

6) The boiling process of the copper foam was modeled as a solid surface similar to a single fin with heat transfer occurring through boiling only on the outer surface because convective heat transfer and mass flux within the foam were assumed negligible. The working fluid within the copper foam exists only as vapor. Depending on the superheat, the average heat transfer coefficient for boiling HFE-7100 from a copper foam surface was found to range between 2,000 and 9,000 $W/(m^2 \cdot K)$. This is similar to the heat transfer coefficient for boiling from the base line surfaces that ranged between 5,000 and 8,000 $W/(m^2 \cdot K)$.

7) Increased aspect ratio in copper-finned microstructures enhances thermal performance for the range of parameters tested (aspect ratio between 9 and 180).

8) For the range of parameters tested for micro-finned structures, decreasing fin density increases thermal performance in the range tested (fin density ranged between 185 and 635 FPI in the present experiments).

9) Copper foams permitted heat removal loads as high as 70 W at a superheat of 90 ^{o}C. The copper foams provided average heat transfer coefficients from the 1 cm^2 footprint ranging from 5,000 to 15,000 W/(m^2·K).

10) Copper-finned microstructures provided heat removal loads up to 43 W at a superheat of 20 ^{o}C. The copper-finned microstructures provided average heat transfer coefficients from the 1 cm^2 footprint ranging from 15,000 to 28,000 W/(m^2·K).

5.1 Recommendations for Future Work

Additional areas in which this work can benefit from further research include the following:

1) An analysis of the heat transfer from outer surfaces of the copper foams by changing the surface tension force relative to the buoyancy force via the use of alternative working fluids (e.g. mixtures of HFE-7100 and HFE-7000) and optimizing the pore diameters for the given fluid.

2) An evaluation of the thermal performance of copper foams with pore densities less than 30 PPI. This would determine if thermal performance decays below a midpoint thickness as suggested by Athreya et al (2002).

3) A study of copper foam thicknesses greater than 5 mm. An optimum thickness may be found by locating a thickness at which thermal performance would begin to decrease.

4) A study of the effect of fin density on thermal performance of copper-finned microstructures for fin densities lower than 185 FPI will facilitate an optimization study to determine the optimal fin density.

5) A study of the thermal performance of both the copper foams and copper-finned microstructures at different footprint sizes to determine the extent by which width and length affect thermal performance of the foams and micro-finned tubes.

6) A multi-objective, multi task optimization study is required to bring non-thermohydraulic parameters in the picture as well. These include parameters such as weight, volume, and mass, as well as cost of the system for a given set of parameters.

REFERENCES

Athreya, B. P., Mahajan., R. L., Sett, S., "Pool Boiling of FC-72 Over Metal Foams: Effect of Foam Orientation and Geometry," Proceedings of the 8th AIAA/ASME Joint Thermophysics and Heat Transfer Conference, June 24 – 26, 2002, St. Louis, MO, pg. AIAA 2002-3214.

Carey, Van P. Liquid-Vapor Phase-Change Phenomena, 1992.

Coursey, Jonathan S. "Performance And Parametric Investigation of a Graphite Foam Thermosyphon Evaporator" University of Maryland, College Park. August 2003.

Goodfellow, 2003, "Nickel/Chromium Technical Data."

Goodfellow, 2003, "Tin/Lead Rosin Solder Technical Data."

Incropera, Frank P., DeWitt, David P., Fundamentals of Heat and Mass Transfer, 5th Edition, August, 2001.

Kalo, Radwan "" University of Maryland, College Park. December 2002.

Patterson, Doug, "Novel Approaches to Conduction Cooling." COTS Journal, pp. 45 –48, May 2002.

Ramaswamy, C., Joshi, Y., Nakayama, W., Johnson, W. B., "Effects of Varying Geometrical Parameters on Boiling from Microfabricated Enhanced Structures," ASME Journal of Heat Transfer, 2003, Vol. 125, pg. 103 – 109.

Stasiulevicius, J., Skrinska, A., Zukauskas, A., Hewitt, G. F., Heat Transfer of Finned Tube Bundles in Crossflow, 1988.

Wong, K. F. and Dybbs, A., "An Experimental Study of Thermal Equilibrium in Liquid Saturated Porous Media," International Journal of Heat and Mass Transfer, 1976, Vol 19, pg. 234 – 235.

3M^{TM}, 2003, "Fluorinert Electronic Liquid FC-72 Product Information."

3M^{TM}, 2003, "Novec Electronic Liquid HFE-7100 Product Information."